

Unprecedented extreme high-frequency radio variability in early-stage active galactic nuclei

E. Järvelä^{1,2}   T. Savolainen^{3,4,5} M. Berton⁶ A. Lähteenmäki^{3,4} S. Kiehlmann^{7,8} T. Hovatta^{3,9} I. Varglund^{3,4} A. C. S. Readhead¹⁰ M. Tornikoski³ W. Max-Moerbeck¹¹ R. A. Reeves¹² and S. Suutarinen^{3,4}

¹*Homer L. Dodge Department of Physics and Astronomy, The University of Oklahoma, 440 W. Brooks St., Norman, OK 73019, USA*

²*European Space Agency (ESA), European Space Astronomy Centre (ESAC), Camino Bajo del Castillo s/n, E-28692 Villanueva de la Cañada, Madrid, Spain*

³*Metsähovi Radio Observatory, Aalto University, Metsähovintie 114, FI-02540 Kylmälä, Finland*

⁴*Department of Electronics and Nanoengineering, Aalto University, PO Box 15500, FI-00076 Aalto, Finland*

⁵*Max-Planck-Institut für Radioastronomie, Auf dem Hügel 69, D-53121 Bonn, Germany*

⁶*European Southern Observatory (ESO), Alonso de Córdova 3107, Casilla 19, Santiago 19001, Chile*

⁷*Institute of Astrophysics, Foundation for Research and Technology-Hellas, GR-70013 Heraklion, Greece*

⁸*Department of Physics, University of Crete, GR-70013 Heraklion, Greece*

⁹*Finnish Centre for Astronomy with ESO, University of Turku, Vesilinnantie 5, FI-20014, Finland*

¹⁰*Owens Valley Radio Observatory, California Institute of Technology, Pasadena, CA 91125, USA*

¹¹*Departamento de Astronomía, Universidad de Chile, Camino El Observatorio 1515, Las Condes, Santiago, Chile*

¹²*Departamento de Astronomía, Universidad de Concepción, Concepción, Chile*

Accepted 2024 July 8. Received 2024 June 7; in original form 2023 September 28

ABSTRACT

We report on the discovery of one of the most extreme cases of high-frequency radio variability ever measured in active galactic nuclei (AGNs), observed on time-scales of days and exhibiting variability amplitudes of 3–4 orders of magnitude. These sources, all radio-weak narrow-line Seyfert 1 (NLS1) galaxies, were discovered some years ago at Aalto University Metsähovi Radio Observatory (MRO) based on recurring flaring at 37 GHz, strongly indicating the presence of relativistic jets. In subsequent observations with the Karl G. Jansky Very Large Array (JVLA) at 1.6, 5.2, and 9.0 GHz no signs of jets were seen. To determine the cause of their extraordinary behaviour, we observed them with the JVLA at 10, 15, 22, 33, and 45 GHz, and with the Very Long Baseline Array (VLBA) at 15 GHz. These observations were complemented with single-dish monitoring at 37 GHz at MRO, and at 15 GHz at Owens Valley Radio Observatory (OVRO). Intriguingly, all but one source either have a steep radio spectrum up to 45 GHz, or were not detected at all. Based on the 37 GHz data, the time-scales of the radio flares are a few days, and the derived variability brightness temperatures and variability Doppler factors are comparable to those seen in blazars. We discuss alternative explanations for their extreme behaviour, but so far no definite conclusions can be made. These sources exhibit radio variability at a level rarely, if ever, seen in AGN. They might represent a new type of jetted AGN, or a new variability phenomenon, and thus deserve our continued attention.

Key words: galaxies: active – galaxies: jets – galaxies: Seyfert – radio continuum: general.

1 INTRODUCTION

Approximately 10 per cent of active galactic nuclei (AGNs) are capable of launching and maintaining relativistic jets (Padovani 2017). Traditionally, these jetted AGNs have been often identified using the radio loudness parameter¹ as a proxy for the jet activity: all the jetted AGNs were believed to be found among the radio-loud population. Whereas the radio loudness parameter might still serve

a purpose when considering bright, high-redshift AGN with steady, powerful jets, and negligible host galaxy contribution, recent studies have shown that it utterly fails when faced with the true diversity of AGN jet phenomenon and variability (Padovani 2017; Lähteenmäki et al. 2018). This is especially problematic in the local Universe, where we are able to detect also lower power jets and outflows in AGN, and where the host galaxy can have a major contribution to the low-frequency radio emission, such that disentangling different sources of radio emission poses a problem (Caccianiga et al. 2015; Järvelä et al. 2017, 2022). This can lead to AGN with low-power relativistic jets to be classified as radio-quiet, or non-jetted AGN with strong star formation to be classified as radio-loud (Caccianiga et al. 2015), making radio loudness a problematic proxy for the jet power and activity.

^{*} E-mail: astrojarvela@gmail.com

[†] Dodge Family Prize Fellow in The University of Oklahoma

¹ Radio loudness parameter, R , is defined as the ratio between 5 GHz flux density and optical B -band flux density. Sources with $R > 10$ are considered radio-loud, $R < 10$ radio-quiet (Kellermann et al. 1989).

Especially one class of AGN, the narrow-line Seyfert 1 (NLS1) galaxies, has played a major role in revealing the diversity seen in AGN activity, and have revolutionized some long-standing assumptions held about AGN. NLS1s are identified based on the optical spectrum: the full width at half-maximum (FWHM) of their broad $H\beta$ emission line is <2000 km s $^{-1}$, and their [O III] emission is weak compared to the broad $H\beta$: $S([O\,III])/S(H\beta) < 3$ (Osterbrock & Pogge 1985; Goodrich 1989). They often also exhibit strong Fe II emission, confirming the unobstructed view of the central engine. The narrow FWHM($H\beta$) can be attributed to low rotational velocity around a low-mass supermassive black hole (10^6 – 10^8 M $_{\odot}$, Peterson 2011; Komossa, Xu & Wagner 2018). The low-mass hypothesis is supported by reverberation mapping studies (Wang et al. 2016; Du et al. 2018), predominantly turbulence-dominated Lorentzian emission-line profiles (e.g. Sulentic et al. 2000; Kollatschny & Zetzl 2011; Berton et al. 2020a), the existence of tidal disruption events (TDEs) in NLS1s (e.g. Frederick et al. 2021), and the prevalence of disc-like host galaxies with pseudo-bulges (e.g. Järvelä et al. 2017; Olgún-Iglesias, Kotilainen & Chavushyan 2020; Varglund et al. 2022). The luminosities of NLS1s, comparable to those of higher black hole mass AGN, such as broad-line Seyfert 1 (BLS1) galaxies, combined with their lower black hole masses indicate that a considerable fraction of NLS1s are accreting close to or even above the Eddington limit (Boroson & Green 1992). This ensemble of properties has led to the conclusion that they are fast-growing, early-stage AGN (Mathur 2000), possibly experiencing one of their first activity cycles.

Based on their properties, NLS1s were not expected to show prominent jet activity, as the ability to launch and maintain powerful relativistic jets was considered to be exclusively a property of massive elliptical galaxies, hosting the most massive black holes (Laor 2000). However, contradictory to this jet paradigm several NLS1s were found to exhibit blazar-like properties in radio band (Komossa et al. 2006; Yuan et al. 2008), and finally the first NLS1 was detected at gamma-rays – indisputably produced by relativistic jets – in 2009 (Abdo et al. 2009). Since then ~ 20 NLS1s have been detected at gamma-rays (Romano et al. 2018; Paliya 2019), and several dozen new candidates have been identified (Foschini et al. 2021, 2022). Furthermore, additional ~ 50 NLS1s have been confirmed to host jets via radio imaging (e.g. Richards & Lister 2015; Lister et al. 2016; Berton et al. 2018; Chen et al. 2020, 2022). NLS1s with relativistic jets share similar properties with the non-jetted NLS1 population and thus broke the jet paradigm beyond any doubt. These jetted NLS1s are also the first AGN with systematically high Eddington ratios to host relativistic jets. Blazars, in general, have Eddington ratios < 0.1 (Heckman & Best 2014), and it was believed that AGN with Eddington ratios significantly higher than that are very rarely capable of launching jets, though some exceptions exist (e.g. Belladitta et al. 2022). Recently, also general relativistic (radiative) magnetohydrodynamics (GRMHD) simulations have shown that efficient and powerful collimated jets are formed in systems with high Eddington ratios, even exceeding unity, if the state of magnetically arrested accretion is reached (McKinney et al. 2017; Liska et al. 2022). Thus it seems that our earlier beliefs regarding relativistic jets were mainly a product of observational biases, for example, concentrating the studies only on the brightest or radio-loudest AGN. It has been suggested that jetted NLS1s represent an early stage of the evolution of jetted AGN and that they will eventually grow into flat-spectrum radio quasars (FSRQ) and radio galaxies (Foschini et al. 2015; Berton et al. 2017). If this is the case, they offer us an unprecedented opportunity to study the very first stages in the evolution of powerful AGN with relativistic jets.

Intriguingly, the radio properties of NLS1s are very diverse: only 15 per cent of them have been detected in radio (Komossa et al. 2006; Järvelä, Lähteenmäki & León-Tavares 2015), and include a continuum of sources from host-dominated to relativistic jet-dominated (Järvelä et al. 2022), whereas the majority of 85 per cent seem to be totally radio-silent. However, NLS1 samples often suffer from misclassifications, and include a significant fraction of BLS1s and intermediate-type AGN that affect the population-wise statistics. Indeed, an ongoing investigation utilizing a carefully selected sample of NLS1s and new radio surveys, such as the LOw-Frequency ARray Two-metre Sky Survey (LoTSS, Shimwell et al. 2022) and the National Radio Astronomy Observatory (NRAO) Very Large Array Sky Survey (VLASS, Lacy et al. 2020), indicate that the radio detection fraction among NLS1s is even lower, around ~ 8 per cent (Varglund et al. submitted). To understand the nature of this seemingly heterogeneous class and how different NLS1s are related, it is necessary to study the population as a whole. Most studies have concentrated on the most obvious radio-bright NLS1s, whereas the radio-faint and -silent population has been scarcely investigated.

1.1 The road so far: 37 GHz observations

A different approach was adopted at the Aalto University Metsähovi Radio Observatory (MRO, Finland), where several hundreds of jetted AGNs are frequently monitored at 37 GHz. In addition to NLS1s that are known to be bright in radio (Foschini et al. 2015; Lähteenmäki et al. 2017), two samples of NLS1s were selected for monitoring based on totally distinct criteria, independent of their radio properties. One sample consisted of NLS1s residing in very dense large-scale (Mpc-scale) environments (Järvelä et al. 2017), and the other was compiled from NLS1s exhibiting spectral energy distributions (SED) that seemed favourable for 37 GHz observations. Järvelä et al. (2017) used luminosity-density fields constructed using luminous red galaxies from the Sloan Digital Sky Survey (SDSS) to study the Mpc-scale environment of a sample of more than 1300 NLS1s. They found that, in general and in agreement with cosmic downsizing, NLS1s reside in low-density regions, such as voids and filaments. On the other hand, more powerful AGNs, such as radio galaxies and blazars, reside in very dense regions, for example, superclusters. Considering the effect of the large-scale environment on the galaxy evolution, it was hypothesized that NLS1s residing in dense environments might be ahead in the evolution compared to their counterparts residing in low-density regions, and might be more likely to harbour jets. Thus, 25 NLS1s residing in supercluster large-scale environments, defined as having the luminosity-density $> 3 \times$ the average, were selected for monitoring. The other sample was selected using two different criteria. First, we selected sources that based on the extrapolation of their SEDs looked like they could be detectable at 37 GHz, and second, we chose sources whose optical or X-ray brightness was unusually high compared to their archival radio detection, indicating that they occasionally could be bright also in radio.

Eight NLS1s from these samples, four from each, were detected at flux density levels of several hundred mJy (Lähteenmäki et al. 2018). What makes these sources extraordinary is that most of them had been deemed to be radio-silent or had only very faint previous radio detections. Seven sources have been detected several times, strongly suggesting that these are genuine detections of recurrent radio flares in these sources. Based on these initial detections and the MRO detection threshold of ~ 200 mJy the amplitude in these sources varies at least by a factor of 2–7 and on a time-scale of days to weeks. The

most likely emission mechanism to produce such high-amplitude, rapid variability at a radio frequency this high is the synchrotron emission of a relativistic jet (however, see Section 5). Additional evidence was obtained when one of the sources was identified as a new gamma-ray emitter and has since been seen brightening in X-rays soon after an MRO-detected flare (Romano et al. 2023).

1.2 Follow-up radio imaging in the *L*, *C*, and *X* bands

Only two of these sources had previous radio detections, and only at mJy levels at 1.4 GHz in the Faint Images of the Radio Sky at Twenty-Centimeters survey (FIRST, Becker, White & Helfand 1995; Helfand, White & Becker 2015) and the NRAO Very Large Array (VLA) Sky Survey (Condon et al. 1998), while the rest were non-detections, meaning their flux densities were below the FIRST detection limit of 1 mJy. To decipher this puzzling behaviour and to discriminate between the different hypotheses of their nature, the sources with several MRO detections were observed with the Karl G. Jansky VLA (JVLA) in A-configuration in *L*, *C*, and *X* bands, that is, at 1.6, 5.2, and 9.0 GHz, respectively. Instead of clarifying the situation, these observations raised more questions. Two of the sources were non-detections and the remaining sources had flux densities ranging from a few tens of μ Jy to a few mJy, all of them consistently showing steep spectra below 9 GHz (see fig. 6 in Berton et al. 2020b). Three of them showed slightly extended radio morphology. In a closer inspection, exploiting spatially resolved spectral index maps, it was found that at least two of these sources show signs of flat core spectrum (Järvelä, Berton & Crepaldi 2021) and thus the presence of a partially optically thick radio core. The JVLA and the MRO observations are not simultaneous, but such an extreme, similar behaviour observed in several sources indicates that it is real, not just a curiosity.

However, the beam size of MRO (\sim 2 arcmin) is considerably larger than the beam size of the JVLA in A-configuration (\sim arcsec scale). It is therefore important to consider the possibility that the discrepancy between the flux densities of the JVLA and MRO could arise from different beam sizes. This seems improbable when taking into account the properties of the emission. Due to the redshift of these sources, the JVLA observations probe kpc-scale structures. The angular sizes of these sources in the optical band are between 2 and 12 arcsec, so we were able to see the whole galaxy in the JVLA observations, in which the smallest field of view – at 9 GHz – was 4.7 arcmin. It is hard to explain such strong and variable radio emission in the outskirts of, or even outside, a galaxy. Due to the rapid variability, indicating a small emitting region, it is highly improbable that resolved-out structures could be responsible for this emission. Furthermore, contamination by nearby sources was ruled out in Lähteenmäki et al. (2018). It can thus be assumed that the JVLA and MRO probe the same phenomenon. The effects of different beam sizes are further discussed in Section 5.2.1.

1.3 Exploring alternative explanations

Since the low-frequency flux densities are consistent with FIRST there is no need to assume that these NLS1s have undergone drastic changes, for example, triggering of jets (Nyland et al. 2020), but it cannot be ruled out either. Thanks to the MRO data we know these sources most likely host relativistic jets, but their radio emission below 9 GHz (*X* band) seems to be consistent with star formation, with little or no contribution from the AGN. Extrapolating, or even assuming a flat radio spectrum up to 37 GHz would mean that in the quiescent state, the flux density would be less than a mJy, which, in the most extreme case, would require a 9000-fold increase

during flares. This would be very extreme, and a more plausible explanation is that the spectrum turns inverted at some point above 9 GHz, as indicated by the MRO data. This kind of behaviour is commonly seen in kinematically young AGN, for example, high-frequency peakers and gigahertz-peaked sources (O’Dea & Saikia 2021). In these sources, the convex radio spectrum is explained by synchrotron self-absorption (SSA) in a young, parsec-scale jet. However, even in these sources, the peak frequency does not usually exceed 10–15 GHz, which in contrast seems to be the case in our sources.

An alternative to SSA could be free–free absorption (FFA), which also allows more inverted spectral indices than SSA (Rodriguez et al. 1993), requiring less extreme variability at 37 GHz. Some cases where the turnover frequency stays consistently high have been found (tens of GHz, Doi et al. 2016), and usually this behaviour is explained by FFA. This could be the case also in these NLS1s: if these sources are kinematically young AGN, FFA could happen in the shocked ionized ambient clouds in front of the jet head (O’Dea & Saikia 2021). Alternatively, the required ionized gas could be provided by the enhanced circumnuclear star formation activity often seen in NLS1s (Sani et al. 2010; Winkel et al. 2022). Either way, these NLS1s with jets that are almost totally absorbed at low radio frequencies seriously challenge the use of the radio loudness parameter as a universal proxy for the jet activity of AGN, and urge us to expand our horizons when it comes to our understanding of the diversity of AGN jets.

To discern between these alternatives, we observed seven of these sources with the JVLA in *X*, *Ku*, *K*, *Ka*, and *Q* bands. These observations were complemented by Very Long Baseline Array (VLBA) observations at 15 GHz, and single-dish observations at 15 and 37 GHz, using the OVRO 40-m telescope and the MRO telescope, respectively. In Section 2, we introduce the sample, in Sections 3.1–3.4, we describe the performed observations, and the data reduction and analysis, in Section 4, we present our results, in Section 5, these results and their implications are discussed, and in Section 6, we provide a brief summary of this work. Throughout this paper, we adopt a standard lambda-cold dark matter cosmology, with a *Hubble* constant $H_0 = 72 \text{ km s}^{-1} \text{ Mpc}^{-1}$, and $\Omega_\Lambda = 0.73$.

2 SAMPLE

The sample includes seven radio-weak NLS1s repeatedly detected at Jy-level flux densities at 37 GHz at MRO. The eighth such source was dropped because it was detected only once. As discussed earlier, these sources were originally selected for the MRO AGN monitoring based on their dense large-scale environments (Järvelä et al. 2017) or SEDs that suggested that they could be detectable at high radio frequencies (Järvelä et al. 2015). The black hole masses were estimated in Järvelä et al. (2015) and Lähteenmäki et al. (2018) using the virial method. Specifically, the estimates are based on the FWHM of the H β line, FWHM(H β), and the monochromatic luminosity at 5100 Å following the relation given in Greene & Ho (2005). The basic properties of the sample are summarized in Table 1.

These sources are very similar to the general NLS1 population: all have a black hole mass less than 10^8 M_\odot (Järvelä et al. 2015; Lähteenmäki et al. 2018), and based on a photometric decomposition of their near-infrared images six of them are hosted in a disc-like host galaxy (Järvelä et al. 2018; Olguín-Iglesias et al. 2020; Varglund et al. 2022), whereas, based on extensive literature search, the morphology of the highest- z source is unknown.

Table 1. Basic properties of the sample.

SDSS name	Short alias	RA (hh mm ss.s)	Dec. (dd mm ss.s)	z	Scale (kpc/arcmin)	$\log M_{\text{BH}}$ M_{\odot}	Large-scale environment	Host
J102906.69+555625.2 ^G	J1029+5556	10 29 06.69	+55 56 25.25	0.451	5.662	7.33	Supercluster	–
J122844.81+501751.2 ^{Ka}	J1228+5017	12 28 44.82	+50 17 51.24	0.262	3.957	6.84	Supercluster	Disc ^c
J123220.11+495721.8 ^X	J1232+4957	12 32 20.12	+49 57 21.82	0.262	3.957	7.30	Supercluster	Disc ^c
J150916.18+613716.7 ^G	J1509+6137	15 09 16.17	+61 37 16.80	0.201	3.235	6.66	Void	Disc ^c
J151020.06+554722.0 ^X	J1510+5547	15 10 20.05	+55 47 22.11	0.150	2.550	6.66	Intermediate	Disc, bar ^a
J152205.41+393441.3 ^{Ka}	J1522+3934	15 22 05.50	+39 34 40.45	0.077	1.420	5.97	Void	Disc, bar, PB ^a , merger
J164100.10+345452.7 ^{Ka}	J1641+3454	16 41 00.10	+34 54 52.67	0.164	2.746	7.15	Intermediate	Disc ^b

Notes. Columns: (1) source name in the SDSS, the superscript indicates the band the coordinates are from, ^G stands for *Gaia*, ^{Ka} for *Ka* band (33 GHz), and ^X for X band (10 GHz); (2) short name; (3) and (4) right ascension and declination (J2000); (5) redshift; (6) scale at the redshift of the source; (7) logarithmic black hole mass, taken from Lähteenmäki et al. (2018); (8) large-scale environment, taken from Järvelä et al. (2017); and (9) host galaxy morphology. PB = pseudo-bulge, taken from ^a Järvelä, Lähteenmäki & Berton (2018), ^b Olguín-Iglesias et al. (2020), and ^c Varglund et al. (2022).

3 DATA

3.1 Karl G. Jansky Very Large Array

3.1.1 Observations and pre-processing

We observed our sample with the JVLA in A-configuration in five different bands, *X*, *Ku*, *K*, *Ka*, and *Q*, centred at 10, 15, 22, 33, and 45 GHz, respectively (Project VLA/22A-002, PI: Järvelä). The dates and integration times of the JVLA observations are given in Table A1. The total bandwidth was 4 GHz in *X*, 6 GHz in *Ku*, and 8 GHz in *K*, *Ka*, and *Q* bands, each band divided to 128 MHz sub-bands, consisting of 64 channels of 2 MHz. The NLS1 (Bertón et al. 2017) 3C 286 was used as the bandpass and flux density calibrator for each source, and each source had an individual nearby, bright source that was used as the complex gain calibrator. The pointing offset calibration was done either at 3C 286 or the current complex gain calibrator. The expected thermal noise levels were 7, 7, 12, 12, and 25 $\mu\text{Jy beam}^{-1}$ in *X*, *Ku*, *K*, *Ka*, and *Q*, respectively. We were able to reach these levels in most cases.

We used the Science Ready Data Products (SRDP) provided by the NRAO. The data were calibrated using the VLA Imaging Pipeline 2022.2.0.64. In addition, the data were checked manually and any remaining bad data were flagged, producing the SRDP measurement set for each source. We also rechecked all the data manually, but no additional flagging was required. In further data processing and analysis, we used the Common Astronomy Software Applications (CASA) version 6.2.1–7. We split the data of our sources from the measurement set separately in each band averaging over time (`timebin` = 10 s) and frequency (`width` = 64, to average 64 channels to form one output channel per sub-band). Before the actual imaging of the targets, we produced radio maps of the size of $2.7 \text{ arcmin} \times 2.7 \text{ arcmin}$, or the whole primary beam, to check the whole beam of the MRO and OVRO telescopes to identify any other sources of radio emission within them. We did not find other strong radio emitters in any of these fields, further supporting the assumption that the radio emission detected at MRO is coming from the NLS1 nucleus.

3.1.2 Radio maps and measurements

We used the `tclean` algorithm with interactive cleaning in CASA to produce the radio images of our sources. The cell size was chosen so that the synthesized beam is properly sampled, meaning a cell size of 250, 150, 100, 70, and 50 mas in *X*, *Ku*, *K*, *Ka*, and *Q* bands, respectively. The image size was chosen so that the whole galaxy fits into the image, taking into account the varying cell sizes in different

Table 2. Summary of the single-dish observations published here.

Name	MRO		OVRO	
	Start date	$N_{\text{det}}/N_{\text{obs}}$	Start date	$N_{\text{det}}/N_{\text{obs}}$
J1029+5556	2014-09-28	3/49	2020-06-30	1/81
J1228+5017	2014-09-08	7/46	2020-06-18	0/93
J1232+4957	2014-04-17	7/66	2020-06-20	0/83
J1509+6137	2014-09-08	23/91	2020-07-09	0/82
J1510+5547	2014-03-19	19/107	2020-06-19	0/75
J1522+3934	2014-05-07	5/129	2020-06-06	4/88
J1641+3454	2014-04-01	12/821	2020-06-05	1/87

Notes. Columns: (1) source name; (2) date the MRO observations were started; (3) number of detections and observations at MRO; (4) date the OVRO observations were started; and (5) number of detections and observations at OVRO.

bands, and the redshifts of our sources. We used Briggs weighting, with `robust` = 1.8, in all cases. Some sources appear to be slightly hexagonal (e.g. J1522+3439), possibly due to the sidelobes. In these cases, we trialled with `robust` values closer to uniform weighting to suppress the sidelobes but there was no visible difference, so we decided to maximize the sensitivity and use the same robustness value for all sources. No source was bright enough to be self-calibrated. We used the `mtmfs` deconvolver with `nterms` = 2 and `scales` = 0 in case some sources would be bright and extended enough to produce spatially resolved in-band spectral index maps, which turned out not to be the case. However, due to this, we did the wide-band primary beam correction separately with `widebandpbcor`.

We fitted each detected source with the CASA task `imfit` using a 2D Gaussian to obtain the central coordinates and the peak flux density and its error. In cases of extended sources we measured the emission inside the 3σ contour, and estimated its error by multiplying the rms by the square root of the emitting region area expressed in beams. The rms for each map was measured in an empty region of sky far from the central source. In case the source was not detected, we report 3σ upper limits. The results are given in Table 3, and the radio maps are shown in Appendix B.

3.2 Very Long Baseline Array

3.2.1 Observations

We observed our sample also on milliarcsecond scale using the VLBA in the *Ku* band, centred at 15.1 GHz (Project BJ 109, PI: Järvelä). The observations were carried out during one 10 h long experiment on 2022 February 08. The recording setup used the Digital Downconverter system of the Roach Digital Backend with

Table 3. Interferometric data for the sample.

Source	Array	Band	Frequency (GHz)	S_{peak} (mJy beam $^{-1}$)	S_{int} (mJy)	Rms ($\mu\text{Jy beam}^{-1}$)	$\nu L_{\nu, \text{peak}}$ ($10^{39} \text{ erg s}^{-1}$)	$\nu L_{\nu, \text{int}}$ ($10^{39} \text{ erg s}^{-1}$)	Beam size ($'' \times ''$)	Beam PA (deg)
J1029+5556	JVLA	X	10.0	< 0.021		7			0.321×0.213	-85.0
	JVLA	Ku	15.0	< 0.015		5			0.222×0.150	-82.3
	JVLA	K	22.0	< 0.024		8			0.145×0.104	-84.3
	JVLA	Ka	33.0	< 0.036		12			0.097×0.082	74.0
	JVLA	Q	45.0	< 0.150		50			0.109×0.089	16.7
	VLBA	Ku	15.1	< 0.348		58			$1.020 \text{ mas} \times 0.550 \text{ mas}$	-1.8
J1228+5017	JVLA	X	10.0	0.128 ± 0.005	0.129 ± 0.010	7	2.027	2.043	0.294×0.223	88.2
	JVLA	Ku	15.0	0.114 ± 0.006	0.117 ± 0.009	6	2.708	2.779	0.191×0.142	-83.4
	JVLA	K	22.0	0.120 ± 0.007		9	4.181		0.129×0.094	-82.0
	JVLA	Ka	33.0	0.102 ± 0.011		12	5.331		0.083×0.064	-80.2
	JVLA	Q	45.0	< 0.093		31			0.060×0.050	-81.9
	VLBA	Ku	15.1	< 0.348		58			$1.030 \text{ mas} \times 0.570 \text{ mas}$	16.3
	LoTSS		0.144	2.374 ± 0.056	2.948 ± 0.112	53			6.000×6.000	
J1232+4957	JVLA	X	10.0	0.033 ± 0.006		7	0.523		0.240×0.215	-66.2
	JVLA	Ku	15.0	0.018 ± 0.001		5	0.428		0.159×0.141	-56.2
	JVLA	K	22.0	< 0.024		8			0.110×0.091	-61.1
	JVLA	Ka	33.0	< 0.033		11			0.071×0.065	-49.1
	JVLA	Q	45.0	< 0.090		30			0.053×0.052	50.5
	VLBA	Ku	15.1	< 0.348		58			$1.040 \text{ mas} \times 0.580 \text{ mas}$	15.7
	LoTSS		0.144	0.350 ± 0.050	0.348 ± 0.087	51			6.000×6.000	
J1509+6137	JVLA	X	10.0	< 0.021		7			0.261×0.204	43.0
	JVLA	Ku	15.0	< 0.018		6			0.171×0.133	33.4
	JVLA	K	22.0	< 0.027		9			0.116×0.092	37.3
	JVLA	Ka	33.0	< 0.039		13			0.080×0.061	44.6
	JVLA	Q	45.0	< 0.105		35			0.061×0.052	61.0
	VLBA	Ku	15.1	< 0.360		60			$0.980 \text{ mas} \times 0.560 \text{ mas}$	0.1
J1510+5547	JVLA	X	10.0	< 0.024		8			0.240×0.225	49.7
	JVLA	Ku	15.0	< 0.018		6			0.162×0.153	52.1
	JVLA	K	22.0	< 0.027		9			0.109×0.095	48.5
	JVLA	Ka	33.0	< 0.039		13			0.074×0.064	53.6
	JVLA	Q	45.0	< 0.105		35			0.059×0.051	74.0
	VLBA	Ku	15.1	< 0.348		58			$0.940 \text{ mas} \times 0.570 \text{ mas}$	0.1
	LoTSS		0.144	0.521 ± 0.084	0.597 ± 0.164	85			6.000×6.000	
J1522+3934	JVLA	X	10.0	0.214 ± 0.008	0.234 ± 0.014	8	0.274	0.299	0.248×0.213	-88.7
	JVLA	Ku	15.0	0.173 ± 0.007	0.177 ± 0.010	6	0.332	0.339	0.162×0.142	82.4
	JVLA	K	22.0	0.148 ± 0.006		9	0.416		0.114×0.106	50.0
	JVLA	Ka	33.0	0.105 ± 0.010		13	0.443		0.095×0.069	76.8
	JVLA	Q	45.0	< 0.102		34			0.067×0.048	-83.7
	VLBA	Ku	15.1	< 0.348		58			$1.060 \text{ mas} \times 0.560 \text{ mas}$	-4.1
	LoTSS		0.144	5.833 ± 0.075	13.599 ± 0.240	71			6.000×6.000	
	RACS		1.3675	3.346 ± 0.307	3.530 ± 0.551				23.050×8.440	171.7
	VLASS1		3.0	1.040 ± 0.00					2.500×2.500	
	VLASS2		3.0	1.008 ± 0.148	1.957 ± 0.411				2.500×2.500	
J1641+3454	JVLA	X	10.0	0.231 ± 0.012	0.424 ± 0.019	7	1.389	2.549	0.259×0.210	-80.5
	JVLA	Ku	15.0	0.170 ± 0.006	0.209 ± 0.010	5	1.533	1.885	0.174×0.146	-73.6
	JVLA	K	22.0	0.118 ± 0.009		8	1.561		0.117×0.096	-75.9
	JVLA	Ka	33.0	0.082 ± 0.012	0.092 ± 0.014	11	1.627	1.825	0.103×0.065	-84.0
	JVLA	Q	45.0	< 0.099		33			0.071×0.049	-77.9
	VLBA	Ku	15.1	< 0.348		58			$1.090 \text{ mas} \times 0.550 \text{ mas}$	3.0
	LoTSS		0.144	7.464 ± 0.100	13.415 ± 0.462	100			6.000×6.000	
	RACS		1.3675	2.744 ± 0.216	3.377 ± 0.433				19.520×9.650	178.9
	VLASS1		3.0	0.965 ± 0.118	1.385 ± 0.266				2.500×2.500	
	VLASS2		3.0	1.034 ± 0.145	1.942 ± 0.340				2.500×2.500	

Notes. Columns: (1) source; (2) array; (3) band used for the observation; (4) central frequency used for the observation; (5) peak flux density, or an upper limit (3σ for the JVLA and 6σ for the VLBA); (6) integrated flux density; (7) rms level of the observation; (8) peak radio luminosity; (9) integrated radio luminosity; (10) clean beam size, in mas for the VLBA observations; and (11) beam position angle.

four 128 MHz wide sub-bands – giving a total bandwidth of 512 MHz – two circular polarizations, and two-bit sampling, resulting in a total recording rate of 4 Gbps.

Due to the potentially low compact flux densities of the target sources, the observations were carried out using the standard phase-referencing technique, that is, a rapid switching between the target and a nearby calibrator. The phase-reference calibrators together with their distances from the targets, their VLBI scale flux densities, and the used source-switching duty cycles are given in Table A2. Each target source had 38 min total on-source integration time. Bright FSRQs 3C 279 and 3C 345 were observed for two 5 min long scans and for three 3 min long scans, respectively. They were used as fringe finders and, more importantly, as calibrator sources for determining instrumental delays and bandpass shapes. Nine out of ten VLBA antennas participated in the observations since Hancock was out due to a frozen focus/rotation mount.

3.2.2 Data reduction

The recorded station data were correlated with the VLBA DiFX correlator in Socorro using 0.5 MHz wide spectral channels and 1 s correlator integration time. This allows a relatively wide field of view, >4 arcsec from the phase centre, to be searched for compact sources.

The data were calibrated in the Astronomical Image Processing System (AIPS; Greisen 2003) using standard procedures for phase-referencing observations. The calibration started with a priori corrections to the station parallactic angle, updates to the Earth Orientation Parameters, and first-order removal of dispersive ionospheric delays using total electron content maps derived from the Global Navigation Satellite System data. Instrumental delays and phase offsets between sub-bands were removed by fringe-fitting a single scan of the bright calibrator 3C 279. A priori amplitude calibration included corrections to sampler threshold levels by using autocorrelations, bandpass calibration using again a scan on 3C 279, and conversion of raw correlator coefficients to Janskys by applying measured system temperatures and gain curves.

The phase reference calibrators as well as the bright calibrators 3C 279 and 3C 345 were fringe-fitted using the AIPS task FRING and combining sub-bands and using an integration time of either 2 min or the scan length, whichever was shorter. The fringe-fitting gave excellent results; the percentage of failed solutions was typically ~ 1 per cent. The fringe-fitting solutions from the phase-reference calibrators were applied to both the calibrators and the target sources. The relative R-L delays were corrected by cross-hand fringe-fitting of a single scan of 3C 279. After this step, we imaged the calibrator data in DIFMAP (Shepherd 1997) and loaded the images back to AIPS. The calibrator images were used to derive phase self-calibration solutions for the calibrator data using the AIPS task CALIB and 10 s integration times. These phase solutions were then applied to the target sources. As the last correction, we also used the amplitude self-calibration solutions from imaging the bright calibrators 3C 279 and 3C 345 to fine-tune the amplitude calibration for those antennas and sub-bands that had an average amplitude self-calibration solution deviating more than 5 per cent from unity. After this step, the target data were ready for imaging.

3.2.3 Imaging and searching for the target sources

While we had quite accurate a priori positions of the target sources based on the previous JVLA data (positional uncertainties less than 10 mas), we still wanted to search for an area that covers most of

the galaxy in case the variable emission seen in the single-dish data does not come from the JVLA core. To achieve this, for each target source we generated a set of naturally weighted images with a field of view of 820×820 mas that covered an area of $7.4 \text{ arcsec} \times 7.4 \text{ arcsec}$ centred on the JVLA position using the multifield option of the AIPS task IMAGR. The image rms was $\sim 60 \mu\text{Jy beam}^{-1}$ for all the target sources which is at the expected thermal noise level. Since we searched for a large area covering one million synthesized beam areas per image, we set the detection threshold to 6σ to avoid picking noise spikes. No sources were detected, and in Table 3, we quote 6σ upper limits for the VLBA data.

3.3 Single-dish data

In addition to radio interferometric data, we obtained non-simultaneous single-dish monitoring data for all of these sources from MRO and OVRO; these data will be published here. These observations are summarised in Table 2 and the detections from these monitoring programmes are shown in Table 4. We also have 1–3 epochs of single-dish observations per source from the Effelsberg 100-m radio telescope between 4.5 and 45 GHz, and one epoch of 2 and 1.15 mm observations with the New IRAM Kids Arrays instrument on the Institut de Radioastronomie Millimétrique (IRAM) 30-m radio telescope on Pico Veleta for five sources. The Effelsberg and IRAM data, complemented by MRO and OVRO data from the same time period, will be published in an upcoming paper.

3.3.1 Metsähovi Radio Observatory

The measurements included in this study are part of the large ongoing AGN monitoring programme at 37 GHz with the 13.7-m radio telescope at MRO. The observations are made with a 1 GHz-band dual beam receiver centred at 36.8 GHz. The beam full-width at half power is 144 arcsec. The observations are on-on observations, alternating the source and the sky in each feed horn. A typical integration time to obtain one flux density data point of a faint source is 1800 s. The sensitivity is limited by sky noise due to the location of the telescope, and it has been experimentally shown that the results do not significantly improve after the maximum integration time of 1800 s. The detection limit of the telescope at 37 GHz is of the order of 200 mJy under optimal conditions. Data points with an S/N (signal-to-noise ratio) < 4 are handled as non-detections. The flux density scale is set by observations of DR 21. Sources NGC 7027, 3C 274, and 3C 84 are used as secondary calibrators. A detailed description of the data reduction and analysis is given in Teräsranta et al. (1998). The error estimate in the flux density includes the contribution from the measurement rms and the uncertainty of the absolute calibration (currently set to 3 per cent). The upper limits are 4σ upper limits based on the measurement rms. Additional details regarding the MRO observations are given in Appendix A2. The data included in this work have been taken between 2014 March and 2022 June.

3.3.2 Owens Valley Radio Observatory

The 15 GHz observations were carried out as part of the general Owens Valley Radio Observatory (OVRO) 40 m radio telescope AGN monitoring programme. This telescope uses off-axis dual-beam optics and a cryogenic receiver with a 15.0 GHz centre frequency and 3 GHz bandwidth. The beam full-width at half power is 157 arcsec. The observations are carried out in on-on fashion to remove

Table 4. Single-dish detections for our sources.

Source	Telescope	Frequency (GHz)	S_{int} (mJy)	Date (dec. yr)
J1029+5556	MRO	37.0	520 ± 80	2016.363276
	MRO	37.0	340 ± 80	2017.402475
	MRO	37.0	400 ± 80	2017.413284
	OVRO	15.0	33.2 ± 3.3	2020.569700
J1228+5017	MRO	37.0	390 ± 60	2015.435445
	MRO	37.0	350 ± 70	2016.412445
	MRO	37.0	480 ± 70	2016.415172
	MRO	37.0	300 ± 70	2016.535148
	MRO	37.0	510 ± 100	2017.404414
	MRO	37.0	470 ± 70	2019.248600
	MRO	37.0	530 ± 100	2019.369877
J1232+4957	MRO	37.0	320 ± 60	2014.290645
	MRO	37.0	410 ± 80	2016.125413
	MRO	37.0	530 ± 70	2016.130824
	MRO	37.0	560 ± 130	2017.40169
	MRO	37.0	370 ± 80	2018.907172
	MRO	37.0	560 ± 90	2019.248668
	MRO	37.0	590 ± 120	2019.89896
J1509+6137	MRO	37.0	670 ± 130	2015.454862
	MRO	37.0	840 ± 140	2015.457565
	MRO	37.0	660 ± 70	2016.396338
	MRO	37.0	480 ± 100	2016.412707
	MRO	37.0	480 ± 100	2016.415428
	MRO	37.0	810 ± 180	2016.418182
	MRO	37.0	510 ± 120	2017.391984
	MRO	37.0	970 ± 140	2017.39745
	MRO	37.0	610 ± 90	2017.413817
	MRO	37.0	450 ± 90	2017.419258
	MRO	37.0	660 ± 120	2017.454812
	MRO	37.0	820 ± 120	2017.473956
	MRO	37.0	820 ± 130	2017.520388
	MRO	37.0	520 ± 100	2018.54222
	MRO	37.0	850 ± 120	2019.012217
	MRO	37.0	1000 ± 160	2019.37014
	MRO	37.0	1020 ± 160	2019.381063
	MRO	37.0	610 ± 110	2019.564088
	MRO	37.0	680 ± 120	2019.698009
	MRO	37.0	700 ± 170	2020.399100
	MRO	37.0	640 ± 130	2020.407293
	MRO	37.0	790 ± 130	2021.725315
	MRO	37.0	620 ± 130	2021.881091
J1510+5547	MRO	37.0	380 ± 80	2015.506706
	MRO	37.0	370 ± 70	2015.784329
	MRO	37.0	510 ± 60	2015.798000
	MRO	37.0	450 ± 90	2015.801756
	MRO	37.0	330 ± 70	2016.396263
	MRO	37.0	490 ± 80	2016.412639
	MRO	37.0	430 ± 80	2016.415360
	MRO	37.0	570 ± 90	2016.418114
	MRO	37.0	290 ± 70	2016.426339
	MRO	37.0	830 ± 140	2016.535468
	MRO	37.0	560 ± 100	2017.056030
	MRO	37.0	340 ± 80	2017.288073
	MRO	37.0	360 ± 90	2017.413749
	MRO	37.0	530 ± 90	2017.41666
	MRO	37.0	350 ± 90	2018.165158
	MRO	37.0	740 ± 110	2018.457715
	MRO	37.0	390 ± 60	2018.531227
	MRO	37.0	370 ± 80	2018.637850
	MRO	37.0	590 ± 110	2019.569528

Table 4 – continued

Source	Telescope	Frequency (GHz)	S_{int} (mJy)	Date (dec. yr)
J1522+3934	MRO	37.0	360 ± 70	2014.397397
	MRO	37.0	300 ± 60	2017.071323
	MRO	37.0	1430 ± 120	2017.221661
	MRO	37.0	280 ± 60	2018.110510
	MRO	37.0	540 ± 110	2021.960079
	OVRO	15.0	7.5 ± 1.7	2020.430300
	OVRO	15.0	45.3 ± 3.0	2020.875700
	OVRO	15.0	23.3 ± 1.9	2021.872600
J1641+3454	OVRO	15.0	19.9 ± 2.0	2021.872600
	MRO	37.0	460 ± 80	2015.993015
	MRO	37.0	280 ± 70	2018.208142
	MRO	37.0	370 ± 90	2019.643459
	MRO	37.0	650 ± 120	2019.684388
	MRO	37.0	380 ± 90	2020.395579
	MRO	37.0	510 ± 110	2020.399177
	MRO	37.0	490 ± 120	2021.265503
J1641+3454	MRO	37.0	480 ± 110	2021.281906
	MRO	37.0	480 ± 90	2021.689678
	MRO	37.0	350 ± 80	2021.779156
	MRO	37.0	430 ± 100	2022.172608
	OVRO	15.0	30.5 ± 3.3	2021.842500

Notes. Columns: (1) source; (2) telescope; (3) central frequency of the observation; (4) flux density and its error; and (5) date of the observation.

atmospheric and ground contamination. In 2014 May, a new pseudo-correlation receiver was installed on the 40 m telescope and the fast gain variations are corrected using a 180-deg phase switch. Calibration is achieved using a temperature-stable diode noise source to remove receiver gain drifts and the flux density scale is derived from observations of 3C 286 assuming the Baars et al. (1977) value of 3.44 Jy at 15.0 GHz. The systematic uncertainty of about 5 per cent in the flux density scale is included in the error bars. The upper limits are 4σ upper limits based on the measurement rms. Complete details of the reduction and calibration procedure are found in Richards et al. (2011) and more details specific to the NLS1 observations are given in Appendix A3.

These seven sources were added to the OVRO AGN monitoring programme in 2020 July, and since then three of them have been detected with $S/N > 4$. This paper includes OVRO data until 2022 June.

3.4 Archival data

In addition to the new data obtained, we also used already published and archival data. First, we included the JVLA A-configuration L -, C -, and X -band data from Berton et al. (2020b) taken in 2019 September. Then, we used the High Energy Astrophysics Science Archive Research Center's (HEASARC) Xamin² to search for any archival radio detections of our sources. From this search, the only detections were the already known FIRST 1.4 GHz detections of J1522+3934 and J1641+3454. In addition, we queried the LoTSS Data Release 2 (DR2) at 144 MHz (Shimwell et al. 2022), TIFR Giant Metrewave Radio Telescope (GMRT) Sky Survey (TGSS) (Intema et al. 2017) at 150 MHz, the Rapid Australian Square Kilometre Array Pathfinder (ASKAP) Continuum Survey (RACS-mid) at 1367.5 MHz (Duchesne et al. 2024), and the NRAO VLASS at 3 GHz (Gordon et al. 2021). Of these, LoTSS, RACS-mid, and

²<https://heasarc.gsfc.nasa.gov/xamin/>

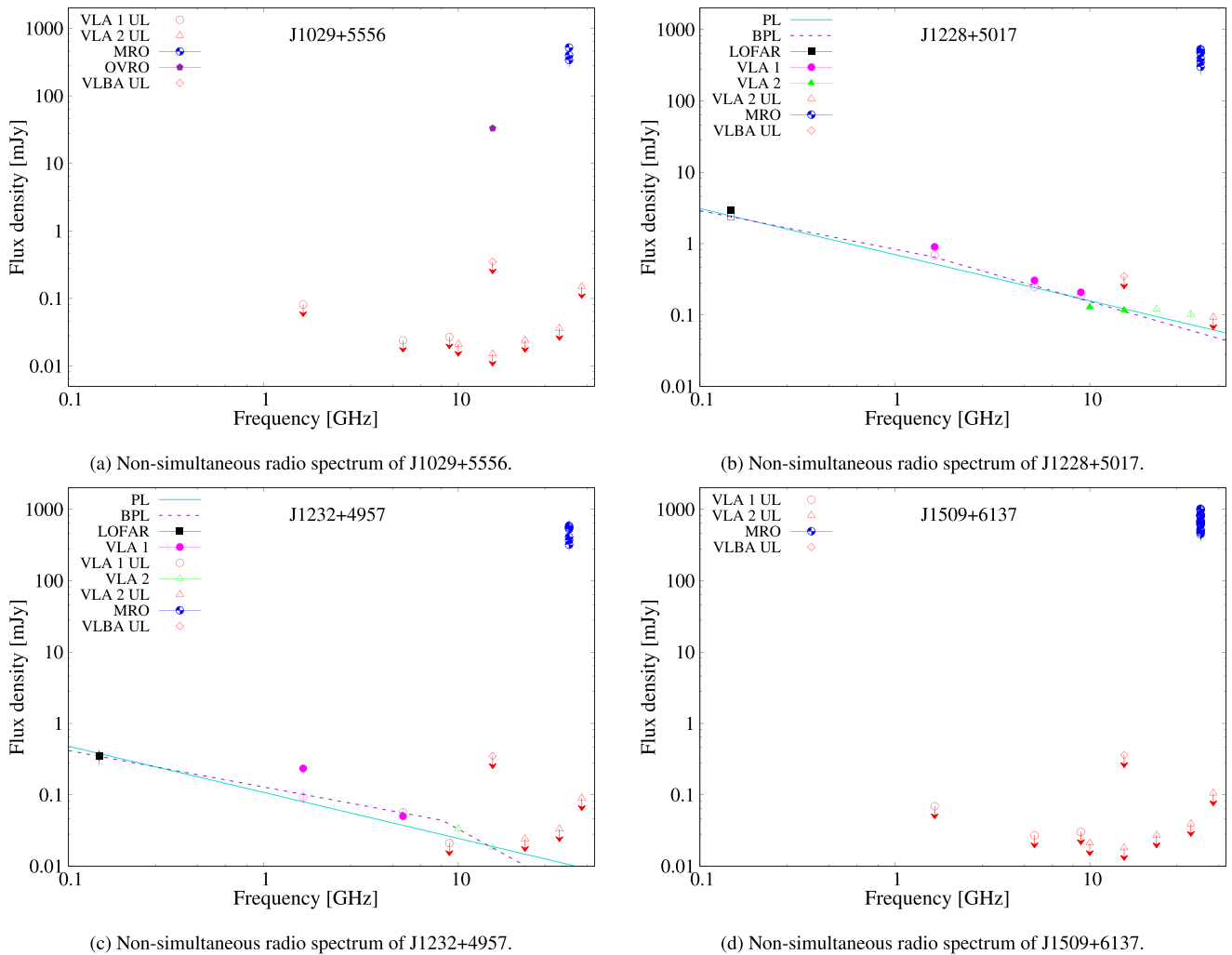


Figure 1. Symbols explained in the figures. Filled symbols denote integrated flux densities and empty symbols mark peak flux densities, except empty symbols with downward arrows that are used for upper limits. VLA 1 data from Berton et al. (2020b) and VLA 2 data from this paper. The PL and BPL fits shown are the fits to the peak flux densities.

VLASS yielded detections. These data are discussed in detail in the individual source sections and the detections are shown in Table 3.

LoTSS has a central frequency of 144 MHz (band 120–168 MHz). All of our sources reside within the published region of the sky. The resolution of LoTSS DR2 is 6 arcsec, the median rms sensitivity is $83 \mu\text{Jy beam}^{-1}$, the flux density scale accuracy is ~ 10 per cent, and the astrometric accuracy is 0.2 arcsec. We used a 1.2 arcmin search radius to check the whole MRO beam area. In addition, we checked the Stokes I continuum radio maps to correctly identify the NLS1, and any other possible radio sources, and to visually cross-match the radio sources with any optical/near-infrared sources using Panoramic Survey Telescope and Rapid Response System (Pan-STARRS) DR1 (Chambers et al. 2016), Two Micron All Sky Survey (2MASS, Skrutskie et al. 2006), *Wide-field Infrared Survey Explorer* (WISE) allWISE Release (Wright et al. 2010), and *Infrared Astronomical Satellite* (IRAS) Improved Reprocessing of the IRAS Survey³ data (Neugebauer et al. 1984; Miville-Deschénes & Lagache 2005). RACS-mid has a central frequency of 1367.5 MHz, with an effective bandwidth of 144 MHz. The median resolution for the

survey is $11.2 \text{ arcsec} \times 9.3 \text{ arcsec}$, but it changes as a function of elevation, being the highest close to the zenith and lowest at low elevations. The median rms noise of RACS-mid is $200 \mu\text{Jy PSF}^{-1}$. We used the same search radius as for LoTSS.

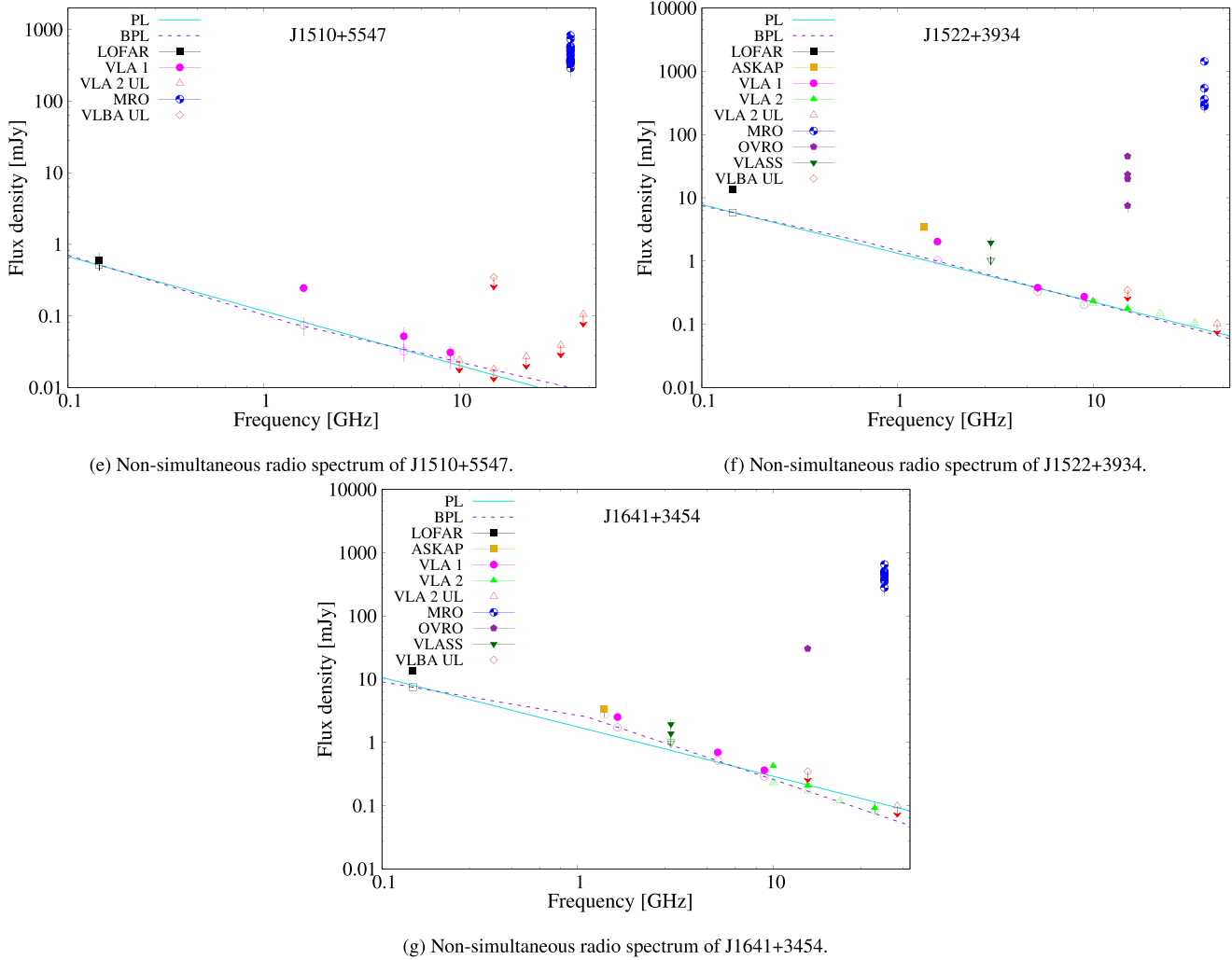
Last, we included NRAO VLASS Epoch 1 and 2 data. The angular resolution of VLASS is ~ 2.5 arcsec, and it covers the entire sky north of $\delta = -40$ deg. In this paper, we use data based on the Quick Look and single epoch imaging, which have a systematic ~ 15 per cent underestimation of the flux density values at $S_{\text{peak}} > 3 \text{ mJy beam}^{-1}$. We used the same search radius as for LoTSS.

4 RESULTS AND ANALYSIS

The results for each source are given in the following sections. All the radio spectra are shown in Fig 1a–g, interferometric data are available in Table 3, and single-dish data in Table 4. In addition to the radio map measurements, we calculated the redshift- and k -corrected radio luminosities as:

$$\nu L_\nu = \frac{4\pi \nu S_\nu d_L^2}{(1+z)^{1+\alpha}} \quad [\text{erg s}^{-1}], \quad (1)$$

³<https://www.ipac.caltech.edu/doi/irsa/10.26131/IRSA94>

Figure 1. *continued.*

where ν is the central frequency of the band in Hz, S_ν the observed flux density in $\text{erg s}^{-1} \text{cm}^{-2} \text{Hz}^{-1}$, d_L^2 the luminosity distance in cm, and α the spectral index of the emission. For simplicity, we used $\alpha = 0$ in all calculations. Even drastic changes in α do not significantly affect the luminosity, that is, the order of magnitude remains the same. Furthermore, since our sources are variable they do not have a characteristic spectral index. The luminosities are given in the Tables in the following sections for individual sources.

Since our sources are only marginally extended or point-like and their JVLA spectra show a consistent slope throughout the detected bands, it is unlikely that in-band spectral index maps could yield significant new information regarding their spectral properties. Thus, we calculated only the traditional spectral indices between new detections with interferometric arrays using both the peak flux densities and the integrated flux densities. These results are shown in Table 5.

Additionally, we fit the data, peak and integrated flux densities separately, with a power law (PL) and a broken power law (BPL). We chose to use a BPL instead of a model with spectral curvature since we do not see strong curvature, such as in peaked sources, in any of our sources, and thus it is not likely that using a spectral curvature model would yield better or more informative results than the BPL model. We modelled the spectra with `scipy.optimize.curve_fit`,

taking the errors into account. For the PL, we fit the usual function $S(\nu) = A \times \nu^\alpha$, (2)

where $S(\nu)$ is the flux density at frequency ν , A is a constant, and α is the spectral index. For the BPL, we used a function of the form

$$S(\nu) = \begin{cases} A \times \left(\frac{\nu}{\nu_b}\right)^{\alpha_1} & \text{when } \nu < \nu_b \\ A \times \left(\frac{\nu}{\nu_b}\right)^{\alpha_2} & \text{when } \nu \geq \nu_b \end{cases} \quad (3)$$

where ν_b is the break frequency, α_1 is the spectral index at frequencies lower than ν_b , and α_2 at frequencies higher than ν_b . Sources J1029+5556 and J1509+6137 do not have enough data to perform either of the fits. For the remaining sources, we extracted the errors associated with the PL fit from the resulting covariance matrix. We were able to reach reasonable BPL fits for J1228+5027, J1232+4957, J1510+5547, J1522+3934, and J1641+3454, but the fit is not well constrained in any of these cases and very similar χ^2 values can be achieved with several different combinations of the parameters. For these fits, we used initial parameters based on the traditional spectral indices and by visually estimating the break frequency. Due to this degeneracy the error estimates for the BPL are not reliable and we instead report the χ^2 value. In the radio spectrum plots, we show the PL and BPL fits for the peak flux densities since we are more interested in the core spectral indices,

Table 5. Spectral indices for our sample.

Source	Frequency	α_{peak}	α_{int}	Δt
J1228+5017	(GHz)			(a)
	0.144–10.0	-0.69 ± 0.01	-0.74 ± 0.03	1–4
	10.0–15.0	-0.29 ± 0.23	-0.24 ± 0.38	0
	15.0–22.0	0.13 ± 0.29		0
J1232+4957	22.0–33.0	-0.40 ± 0.41		0
	0.144–10.0	-0.56 ± 0.08		1–4
	10.0–15.0	-1.49 ± 0.59		0
J1522+3934	0.144–3.0	-0.58 ± 0.05	-0.64 ± 0.07	0–2
	3.0–10.0	-1.29 ± 0.15	-1.76 ± 0.22	2.5
	10.0–15.0	-0.52 ± 0.19	-0.69 ± 0.29	0
	15.0–22.0	-0.41 ± 0.21		0
	22.0–33.0	-0.85 ± 0.33		0
J1641+3454	0.144–3.0	-0.65 ± 0.05	-0.64 ± 0.07	0–2
	3.0–10.0	-1.24 ± 0.16	-1.26 ± 0.18	2.5
	10.0–15.0	-0.76 ± 0.22	-1.74 ± 0.23	0
	15.0–22.0	-0.95 ± 0.29		0
	22.0–33.0	-0.90 ± 0.55		0

Notes. Columns: (1) source; (2) frequencies used, 0.144 GHz data from LoTSS and 3.0 GHz data from VLASS, other data from this paper; (3) spectral index using peak flux densities; (4) spectral index using integrated flux densities; and (5) time difference between the observations, except in case of LoTSS DR2 a time range since the exact times of observations are not known.

which are more likely to have a significant contribution from the AGN. Furthermore, we do not know if any extended emission is resolved-out at higher frequencies, possibly causing underestimated integrated flux densities. Thus, using the peak flux densities is more consistent. All the results are available in Table 6.

Due to the nature of these sources, it is hard to properly quantify their variability. Commonly used variability metrics, such as the modulation index or fractional variability, are based on detections, and cannot properly account for upper limits or non-detections. In our case, the non-detections, detections at a different frequency (15 GHz at OVRO), and detections with a different instrument (JVLA) play a crucial role in estimating the strength of the variability. Employing, for example, the modulation index, would drastically underestimate the amplitude of the variability in our sources. However, to give an order of magnitude estimate of the variability we simply calculated by which factor the JVLA *Ka*-band flux density needs to increase to reach the maximum flux density detected at 37 GHz (shown in

Table 7. Maximum variability of the sources, indicated by the factor the *Ka*-band flux density needs to increase to reach the maximum flux density at 37 GHz.

Source	Multiplying factor	Lower limit?
J1029+5556	14 444	Yes
J1228+5017	5196	No
J1232+4957	17 879	Yes
J1509+6137	26 154	Yes
J1510+5547	21 282	Yes
J1522+3934	13 619	No
J1641+3454	7927	No

Notes. Columns: (1) source; (2) multiplying factor; and (3) lower limit.

Table 7). We note that this is by no means ideal due to the use of different instruments and frequencies.

Additionally, we used temporally close consecutive 37 GHz detections to estimate the properties of the flares. The details of the calculations and the results are given in Section 4.8, but referred to in the following sections for the individual sources.

4.1 SDSS J102906.69+555625.2

So far J1029+5556 has been detected at 37 GHz at MRO and at 15 GHz at OVRO (Table 4). It has not been detected in any radio interferometric observations (see Table 3). Based on the *Ka*-band upper limit and the maximum 37 GHz flux density, its flux density should have increased at least by a factor of $\sim 14\,000$ to account for this flare. J1029+5556 has the highest redshift, $z = 0.451$, in this sample, and due to this it is also the only source that, based on literature search, is missing the host galaxy morphology information. Varglund et al. (2022) attempted to model the host using near-infrared images obtained with the Nordic Optical Telescope but the results remain inconclusive due to non-optimal seeing coupled with the high redshift of the source, preventing properly resolving the galaxy. Interestingly, it was detected at MRO only three times in 2016–2017, with moderate flux densities around 500 mJy and below, and has not been detected after that, though it has not been observed very frequently in the past few years. Its overall detection percentage at 37 GHz is 6.1 per cent, and the mean luminosity $\nu L_\nu = 9.5 \times 10^{43}$ erg s $^{-1}$. The lack of recent detections might indicate a change in the activity level of the nucleus, though it was detected by OVRO in 2020, indicating that the activity has not totally halted. Whether the amplitude of the variability has changed or if the most drastic variability has moved to lower frequencies cannot be determined

Table 6. Parameters of PL and BPL fits to the radio spectra of our sources.

Source	Peak flux densities						Integrated flux densities					
	PL		BPL				PL		BPL			
	α	α_1	α_2	ν_{break} [GHz]	χ^2 (d.o.f.)		α	α_1	α_2	ν_{break} [GHz]	χ^2 (d.o.f.)	
J1029+5556	Not enough data for either fit											
J1228+5017	-0.65 ± 0.03	-0.54	-0.78	1.57	0.05 (5)	-0.68 ± 0.04	-0.49	-0.97	1.82		0.01 (3)	
J1232+4957	-0.65 ± 0.05	-0.51	-1.5	8.3	<0.01 (2)	-0.55 ± 0.24				Not enough data		
J1509+6137	Not enough data for either fit											
J1510+5547	-0.76 ± 0.03	-0.83	-0.63	1.41	<0.01 (1)	-0.72 ± 0.15	-0.29	-1.22	1.28		<0.01 (1)	
J1522+3934	-0.77 ± 0.02	-0.68	-0.82	0.67	4.65 (7)	-0.94 ± 0.02	-0.79	-1.12	1.37		1.82 (5)	
J1641+3454	-0.78 ± 0.03	-0.53	-1.04	1.12	0.26 (8)	-0.88 ± 0.04	-0.66	-1.09	1.36		0.38 (7)	

Notes. Columns: (1) source; (2)–(6) fit parameters using peak flux densities: (2) PL slope; (3) BPL slope below the break frequency; (4) BPL slope above the break frequency; (5) break frequency; (6) χ^2 for the BPL fit, degrees of freedom in parentheses; (7)–(11) fit parameters using integrated flux densities: (7) PL slope; (8) BPL slope below the break frequency; (9) BPL slope above the break frequency; (10) break frequency; and (11) χ^2 for the BPL fit, degrees of freedom in parentheses.

based on these data. J1029+5556 is not present in LoTSS maps, but there is one radio source, which lacks an optical/infrared counterpart, in the LoTSS map within the MRO beam. However, the source is faint, with a flux density of ~ 1 mJy, and we do not see signs of it in the JVLA data. The non-simultaneous radio spectrum of J1029+5556 is shown in Fig. 1(a) and the light curves in Figs C1 and C8.

4.2 SDSS J122844.81+501751.2

J1228+5017 is detected with the JVLA in all other bands except the Q band, and it is also detected in LoTSS at 144 MHz (Table 3). It is only marginally resolved or unresolved in all JVLA bands (Figs B1–B5). In the 144 MHz radio map, it seems to be extended toward north-west, but upon closer inspection, the extended part turns out to be a nearby galaxy that can also be seen in optical images. The radio spectrum, shown in Fig. 1(b), has a slope around -0.7 from 144 MHz to X band, above which the slope flattens considerably (Table 5). The low-frequency spectral index is consistent with the characteristic star formation activity spectral index of -0.7 and the flux density levels could be explained by star formation, as found in Berton et al. (2020b) who estimated the low-frequency radio emission produced by star formation using mid-infrared data. However, it should be noted that also the spectral index of optically thin synchrotron emission by shock-accelerated electrons in jets is around -0.7 . The spectrum shows the characteristic spectral turnover, or spectral index flattening, toward lower frequencies where the emitting medium starts to become opaque to radio emission (Condon 1992). Indeed, the BPL fit (Table 6) finds a break frequency around 1.6 GHz, indicating a complex spectral shape. In principle, the high-frequency spectral index is very close to the thermal free–free emission spectral index of -0.1 , which in star-forming galaxies has an increasing contribution toward higher frequencies, whereas the steep synchrotron emission from supernovae becomes less important. However, the change in the slope between the non-thermal and thermal emission-dominated spectral regions should not be this drastic (Klein, Lisenfeld & Verley 2018). Instead, the flattening could be due to a third component, the flat radio core of the AGN that becomes detectable when the emission produced by star formation weakens. Spatially resolved spectral index maps in L , C , and X bands support this scenario since despite the overall steep spectral index, the core spectral index in these bands is significantly flatter (Järvelä et al. 2021). X band also shows a peak flux density decrease from 0.184 ± 0.008 mJy beam $^{-1}$ in Berton et al. (2020b) to 0.128 ± 0.005 mJy beam $^{-1}$ in these observations. The JVLA configuration and the rms of the maps are the same for both observations, but the central frequencies are slightly different (9 versus 10 GHz), thus the difference could be due to the slightly different beam sizes since the source is partially resolved.

J1228+5017 has been detected at MRO seven times, with the last detection in 2019, and has a detection percentage of 15.2 per cent and a mean luminosity of $\nu L_\nu = 2.6 \times 10^{43}$ erg s $^{-1}$. The account for the highest amplitude 37 GHz flare the flux density of J1228+5017, based on the Ka -band data, should have increased by a factor of ~ 5000 . The single-dish detections are listed in Table 4 and the light curves are shown in Figs C2 and C9. However, the source does not seem to have totally gone into slumber as it has been detected again recently (Järvelä et al. in preparation).

4.3 SDSS J123220.11+495721.8

In the earlier JVLA observations, J1232+4957 was detected in L and C bands, but not in X band. In the new observations, it is also detected in X and Ku bands, but only at a 3σ level (Table 3).

J1232+4957 is also detected in LoTSS at 144 MHz. It remains unresolved in all interferometric observations (Figs B6 and B7). Its radio spectrum, in Fig. 1(c), clearly shows a steepening slope toward higher frequencies. The spectral index between 144 MHz and X band is -0.56 ± 0.08 , and between X and Ku bands -1.49 ± 0.59 (Table 5). The BPL clearly fits the data better than the simple PL (Table 6), finding a spectral index of -0.51 below the break frequency of 8.3 GHz, and a much steeper spectral index of -1.50 above it. The interferometric flux densities of J1232+4957 can be explained by star formation activities, as shown in Berton et al. (2020b), and thus AGN contribution does not seem necessary. However, the drastic drop with a very steep spectral index above the break frequency is unusual in purely star-forming galaxies (Klein et al. 2018), and might be indicative of electron ageing, hinting at a non-thermal origin.

On the other hand, J1232+4957 has been detected at MRO several times with an overall detection percentage of 10.6 per cent. The mean luminosity of the detections is $\nu L_\nu = 2.8 \times 10^{43}$ erg s $^{-1}$. The last detection, however, is from 2019 (Table 4). The 37 GHz flux densities are quite modest, never exceeding 600 mJy. However, due to the upper limit in Ka band, the flux density of J1232+4957 should have increased at least by a factor of ~ 17000 to explain the maximum flux density at 37 GHz. The light curves of J1232+4957 are shown in Figs C3 and C10.

4.4 SDSS J150916.18+613716.7

J1509+6137 is an intriguing source as it has clearly the highest detection percentage at 37 GHz – 25.3 per cent – but it has not been detected in any JVLA band. The MRO detections have an average luminosity of $\nu L_\nu = 2.5 \times 10^{43}$ erg s $^{-1}$. The light curves are shown in Figs C4 and C11, and the radio data are given in Tables 3 and 4. The brightest MRO flares exceed 1 Jy, indicating extreme variability of at least four orders of magnitude when compared to the Ka -band upper limit. J1509+6137 also has several double detections within a week of each other. These detection pairs were used to estimate the flare characteristics (Table 8) and are discussed in Section 4.8.

J1509+6137 was not detected in LoTSS, but there are two other radio sources within the MRO beam in LoTSS. Neither of these sources have optical/infrared counterparts, and both of them are faint, around 0.4 and 0.8 mJy. They are not seen in the JVLA data. J1509+6137 seems to be totally absent in radio – except during the 37 GHz flares – and does not even show detectable amounts of radio emission from star formation.

4.5 SDSS J151020.06+554722.0

J1510+5547 has a high detection percentage of 17.6 per cent at 37 GHz (Table 4 and Figs C5 and C12). It was last detected in 2019 even if the number of annual observations has stayed roughly the same. The mean luminosity at 37 GHz is $\nu L_\nu = 8.7 \times 10^{42}$ erg s $^{-1}$. It was detected in L , C , and X bands in our previous JVLA observations, but remained a non-detection in all bands, X through Q , in the recent observations (Table 3). Considering the Ka -band upper limit the variability needs to be at least four orders of magnitude to explain the maximum flux density at 37 GHz. The radio spectrum of J1510+5547 is shown in Fig. 1(e), and the PL fit to the peak flux density values suggests a spectral index around -0.7 or slightly steeper (Table 6). The integrated flux density spectrum seems to bend and indeed the BPL fit indicates a break frequency around 1.28 GHz and spectral indices of -0.29 and -1.22 below and above it, respectively. The X -band upper limit is very close to the earlier X -band detection flux density. It appears that the difference of 1 GHz

Table 8. Flare properties from the MRO data.

Source	Start time (dec. yr)	Stop time (dec. yr)	S_{begin} (Jy)	S_{end} (Jy)	τ (d)	$T_{\text{b, var}}$ (10^{14} K)	δ_{var}
Rising							
J1509+6137	2016.415428	2016.418182	0.48 ± 0.10	0.81 ± 0.18	$2.0^{+13.1}_{-0.9}$	$17.2^{+55.1}_{-16.9}$	$32.5^{+20.0}_{-24.4}$
J1509+6137	2017.391984	2017.397450	0.51 ± 0.12	0.97 ± 0.14	$3.2^{+4.4}_{-2.8}$	$8.0^{+16.7}_{-6.8}$	$25.2^{+11.5}_{-11.9}$
decaying							
J1509+6137	2017.397450	2017.413817	0.97 ± 0.14	0.61 ± 0.09	$13.2^{+24.6}_{-5.2}$	$0.5^{+1.0}_{-0.4}$	$9.7^{+4.5}_{-5.2}$

Notes. Columns: (1) source; (2) and (3) start and stop times of the flare; (4) and (5) flux density at the beginning and at the end of the flare; (6) time-scale; (7) variability brightness temperature; and (8) variability Doppler factor.

between the central frequencies of these two X -band observations and the steep spectral index is enough to cause the non-detection in these recent observations.

This source is also detected in LoTSS and seems to be marginally resolved. There is another radio source north-east of it and within the MRO beam. This source is faint, has no optical/infrared counterpart, and is not seen in any JVLA band. The projected distance between J1510+5547 and the source is more than 40 kpc, thus it is unlikely that it is related to our source. Based on Berton et al. (2020b), the radio spectrum below 10 GHz could be explained by star-forming activity, but with these data only it is impossible to say if also an AGN contributes, and which one is the predominant source of this radio emission.

4.6 SDSS J152205.41+393441.3

J1522+3934 is a nearby source ($z = 0.077$) that resides in a disc galaxy that is merging with a non-active galaxy (Järvelä et al. 2018). It shows almost symmetrical resolved emission on west/north-west and east/south-east sides of the nucleus from 144 MHz to Ku band, and is detected up to Ka band (Table 3 and Figs B8–B11). Interestingly, the extended radio emission is perpendicular to the optical host galaxy, indicating that it does not originate from the star formation activity in the host (Järvelä et al. 2021). To explain the 37 GHz flaring in J1522+3934 the jet emission needs to be relativistically boosted as, according to our current knowledge, this kind of variability amplitudes cannot be explained by intrinsic non-boosted variability. Following this, we can deduce that the jet or parts of it need to point close to our line of sight. If this is the case, the extended emission would be a relic of past activity – unless the jets are very bent, pointing at us close to the nucleus and turning perpendicular at larger distances. The spatially resolved spectral index map in the L band does show regions of steeper spectral index around -1.0 , possibly indicative of synchrotron cooling (Kardashev 1962; Komissarov & Lubanov 1994).

The radio spectrum of J1522+3934, in Fig. 1(f), has a slope around -0.8 when fit to the peak flux densities and somewhat steeper, around -0.9 when using the integrated flux densities (Tables 5 and 6). The VLASS points seem to deviate from this which is surprising considering that the Quick Look flux densities should underestimate the real flux densities. Also the RACS flux density seems to lie above the level of the JVLA observations. In principle, the discrepancy could be explained by resolved-out emission in the JVLA A-configuration observations. However, in JVLA L band, between RACS and VLASS, the largest angular scale is 36 arcsec, corresponding to > 50 kpc, so it is unlikely that there would be a lot of resolved-out emission. Overall the spectrum seems to be consistent with optically thin radio emission and we can assume its predominant origin to be the AGN.

J1522+3934 has the record 37 GHz flux density among our sources at 1430 mJy, whereas the other detections are much more modest. Based on the Ka -band flux density four orders of magnitude of variability is required to explain the brightest flare at 37 GHz. Its detection percentage at MRO is only 3.9 per cent, and the mean luminosity is $\nu L_{\nu} = 2.7 \times 10^{42}$ erg s $^{-1}$. In addition to these detections, it has also been detected at 15 GHz at OVRO on three different dates (Table 4), with a maximum flux density of 45 mJy. The light curves of J1522+3934 are shown in Figs C6 and C13.

4.7 SDSS J164100.10+345452.7

J1641+3454 is the only one of our sources with a statistically significant gamma-ray detection (Lähteenmäki et al. 2018), usually considered as proof of the presence of relativistic jets. Interestingly, its detection rate at 37 GHz is the lowest in the sample at 1.5 per cent. Its 37 GHz flux densities are modest, generally around 500 mJy and below, indicating that most of its flaring activity might not exceed the MRO detection threshold. Its average 37 GHz luminosity is $\nu L_{\nu} = 9.9 \times 10^{42}$ erg s $^{-1}$. J1641+3454 has also been detected at 15 GHz at OVRO with a flux density of ~ 30 mJy (Table 4).

J1641+3454 was a target of an intense 20-month multiwavelength monitoring campaign in radio, optical, ultraviolet, and X-rays (Romano et al. 2023). During the campaign, it flared twice at 37 GHz: the first radio flare was followed by brightening in X-rays, whereas the latter flare was not accompanied by any significant changes at other frequencies. Nevertheless, this was the first detection of a 37 GHz radio flare counterpart at another frequency.

J1641+3454 is detected in X , Ku , K , and Ka bands with the JVLA (Table 3). Based on the Ka -band measurement flux density variability by a factor of almost ~ 8000 is required to explain the maximum flux density at 37 GHz. J1641+3454 is resolved in X and Ku bands, with extended emission seen on the north-west and the south-east sides of the nucleus. This emission is also seen at lower frequencies and it appears to be patchy, which points to star formation as the origin (Berton et al. 2020b), although diffuse radio emission due to AGN activity cannot be ruled out. J1641+3454 is also detected at 144 MHz in LoTSS, at 1.3675 GHz in RACS, and at 3 GHz in VLASS. At 3 GHz it is not properly resolved but appears elongated in the north-west/south-east direction similarly to the JVLA maps. Interestingly, in the LoTSS map, it seems to be elongated toward south-west. This emission has no optical/infrared counterpart, but it is clearly outside the host galaxy of J1641+3454, so it remains unclear whether it is related to J1641+3454. If it were it could be a relic of past activity, but these data are not enough to draw conclusions either way.

The radio spectrum of J1641+3454, shown in Fig. 1(g), clearly has a curvature, and it flattens towards lower frequencies and steepens toward higher frequencies (Table 5). The BPL fit to the peak flux densities, reported in Table 6, yielded a break frequency of 1.12 GHz,

and a spectral index of -0.53 below it and -1.04 above it. No AGN contribution is required to explain the properties of its low-state radio spectrum, though Berton et al. (2020b) found the low-frequency flux densities to be slightly more than what is expected from star formation activity.

In addition to the 37 GHz detections, J1641+3454 has also been detected once at 15 GHz by OVRO with a flux density of ~ 30 mJy. The OVRO detection is quite close to an MRO detection, within 23 d, but unfortunately in the case of these sources, we cannot assume that these detections are necessarily from the same event. However, in the case they were, we can derive a quasi-simultaneous spectral index of 2.70 ± 0.63 . Since these detections are not strictly simultaneous and we do not know which stage of the flare the detections represent, the spectral index is only a rough estimate. It agrees with the maximum value of the spectral index produced by SSA (2.5, Condon & Ransom 2016) within the errors but might imply that also another source of absorption, such as FFA, is required. The light curves of J1641+3454 are shown in Figs C7 and C14.

4.8 Flare characteristics using MRO data

We can use the consecutive MRO detections to infer some properties of the radio emission in our sources. Following Valtaoja et al. (1999) and Hovatta et al. (2009) we can estimate the flare rise and decay e -folding time-scales, variability brightness temperatures, and variability Doppler factors. We performed these calculations for all consecutive detections – that is, there are no non-detections between them – that were less than seven days apart and had different flux densities even when taking the errors into account. We cannot be sure if the two detections are from the same flare, but in case they are not, it means that the variability is even faster and more extreme. We also assume that the maximum amplitude of the flare is equal to the higher of the two flux densities. In case it is not, and the real amplitude of the flare is larger, the time-scales would be shorter. Thus, these time-scale estimates and the parameters derived from them can be considered as lower limits. For simplicity, since our knowledge of these sources is so limited, we used the same equation for both rising and decaying flares:

$$\Delta S(t) = \Delta S_{\max} e^{(t-t_{\max})/\tau} \quad [\text{Jy}], \quad (4)$$

where ΔS_{\max} is the maximum amplitude of the flare in Jy, after subtracting the baseline flux density level, S_b , t_{\max} is the epoch of the peak of the flare, and τ is the rise or decay time of the flare expressed in days (e -folding time-scale). We do not know the exact quiescent flux density level, but based on the OVRO observations it cannot be much higher than ~ 10 mJy (see Section 5.2.1), so we chose this number as the baseline flux density level. The results are shown in Table 8.

To estimate the variability Doppler factors of our sources, we calculated the variability brightness temperature, $T_{\text{b, var}}$, (in the source proper frame) with:

$$T_{\text{b, var}} = 1.548 \times 10^{-32} \frac{\Delta S_{\max} d_L^2}{\nu^2 \tau^2 (1+z)} \quad [\text{K}], \quad (5)$$

where ν is the observed frequency in GHz, d_L is the luminosity distance in metres, and ΔS_{\max} and τ are defined in equation (4). The numerical factor corresponds to using $H_0 = 72 \text{ km s}^{-1} \text{ Mpc}^{-1}$, and $\Omega_\Lambda = 0.73$, and assuming that the source is a homogeneous sphere. Since estimating the brightness temperature from the flux density variability is based on a causality argument, these values are in fact lower limits. We calculated the variability brightness temperatures for all flares with τ values. It should be kept in mind that the brightness

Table 9. Required Doppler factors and changes in the viewing angle of the jet.

S_0 (mJy)	S_{obs} (mJy)	δ_{stream} $p = 2$	δ_{blob} $p = 3$	$\Delta\theta_{\Gamma=10}$ ($^\circ$)	$\Delta\theta_{\Gamma=20}$ ($^\circ$)
0.05	500	100.0	21.5	–	15.1
0.05	1000	141.4	27.1	–	15.7
0.1	500	70.7	17.1	22.9	14.5
0.1	1000	100.0	21.5	–	15.1
0.2	500	50.0	13.6	21.3	13.8
0.2	1000	70.7	17.1	22.9	14.5

Notes. Columns: (1) unbeamed flux density; (2) beamed flux density; (3) required Doppler factor assuming a continuous jet stream; (4) required Doppler factor assuming a moving component in the jet; (5) required change in the viewing angle assuming $p = 3$ and $\Gamma = 10$; and (6) required change in the viewing angle assuming $p = 3$ and $\Gamma = 20$.

temperatures derived from variability are systematically larger by a factor of δ^2 , where δ is the Doppler factor, than those obtained directly from VLBI measurements due to the different dependence on the Doppler factor.

Once we know the variability brightness temperature we can use it to estimate the variability Doppler factor, assuming we know the intrinsic brightness temperature, $T_{\text{b, int}}$:

$$\delta_{\text{var}} = \left(\frac{T_{\text{b, var}}}{T_{\text{b, int}}} \right)^{1/3}. \quad (6)$$

For the intrinsic brightness temperature, we use 5×10^{10} K (Readhead 1994; Lähteenmäki, Valtaoja & Wiik 1999; Homan et al. 2021), which assumes equipartition between the energy densities of the magnetic field and the radiating particles. However, we do not know if these sources are in equipartition and therefore cannot say how accurate the Doppler factor estimates are. Indeed, the rapid variability suggests that this may not be the case. However, even if the intrinsic brightness temperature deviates from the equipartition brightness temperature by an order of magnitude, the derived Doppler factors would be within the errors of the Doppler factors that assume equipartition.

Keeping these caveats in mind, the results are reported in Table 8. There are three sources with consecutive MRO detections within one week: J1228+5017, J1509+6137, and 1510+5547, but after excluding all the detections that can be the same within the error bars, only one source, J1509+6137, remains. It has shown two rising and one decaying flare that meet our criteria. In all cases the e -folding time-scales are of the order of days or a maximum of a few weeks, the variability brightness temperatures around 10^{14} – 10^{15} K, and the variability Doppler factors between 5 and 50. These parameters, except the time-scale, are comparable to what is seen in FSRQs (Hovatta et al. 2009).

We can use a simple light travelttime argument to infer an approximate size of the radio-emitting region. The size needs to be $r < c\tau\delta/(1+z)$. For τ of 5 d, this gives $0.0042 \text{ pc} \times \delta/(1+z)$ and for 10 d, $0.0084 \text{ pc} \times \delta/(1+z)$. Taking into account the Doppler factor the size of the emitting region can increase by about an order of magnitude, whereas accounting for the redshift decreases the size by ~ 10 per cent–30 per cent. These sizes are rough estimates since we cannot properly estimate the time-scales with the current data, but it is probably safe to assume that the order of magnitude is correct and that the emitting region needs to be milliparsec in size. This indicates that the emission originates close to the black hole, well within the broad-line region (BLR), or from spatially limited regions inside the jet.

5 DISCUSSION

All of their variability properties considered these seven sources exhibit flux density variations at a level never observed in AGN before at high radio frequencies. The short variability time-scales they show are rare, but not unheard of, even in the radio regime (Rani et al. 2013), whereas the amplitude of the variability – 3–4 orders of magnitude – coupled with the short time-scales, is unprecedented to the best of our knowledge. Nyland et al. (2020) report low-frequency variability up to 2500 per cent on decadal time-scales, but this variability seems to be related to the emergence of a new, persistent radio source, for example, due to the onset of the jets. Ross et al. (2022) report on high-amplitude MHz-range variability in a sample of peaked sources, but also in this case the time-scales are of the order of weeks or months.

Based on the 37 GHz light curves (Figs C8–C14), including both detections and upper limits (see Appendix A2 for details), most of the sources are usually detected close to the detection threshold of MRO. However, out of all the detections 39 per cent have $4 < \text{S/N} < 5$, 32 per cent have $5 < \text{S/N} < 6$, and 29 per cent have $\text{S/N} > 6$. J1509+6137 – which has not been detected in interferometric observations at all – is an exception and consistently shows activity that is clearly above the detection limit. In general, there do not seem to be notable trends in the detections, other than that the sources are detected more when they are observed more, which is not surprising. In some sources (e.g. J1228+5017 and J1232+4957) there seem to be higher upper limits crowding around detections, possibly indicating an increased level of activity during that particular epoch (but see Appendix A2 for caveats). In others, such as J1641+3454, the detections are embedded amongst upper limits that show no apparent trends of activity. On the other hand, many detections are not accompanied by other nearby observations at all.

At OVRO all detections, except the first detection of J1522+3934, are clearly above the detection threshold. However, the detectability at 15 GHz compared to 37 GHz might be lower. Only three sources have been detected at 15 GHz and the highest detection rate is only 4.5 per cent. The sources with the highest detection rates at 37 GHz have not been detected at 15 GHz at all despite the comparable number of observations. This might indicate that the flaring behaviour is stronger, in terms of the amplitudes, towards higher frequencies. Though, it should be noted that for many sources most MRO detections are from the time before OVRO started monitoring them, so it is also possible that these sources have been less active throughout the OVRO observations.

For some sources (J1509+6137, J1522+3934, and J1641+3454), there are a few MRO detections with OVRO observations within $\sim 1\text{--}5\text{ d}$ before or after the MRO detection. Using these detections and the OVRO upper limits, these quasi-simultaneous observations can be used to estimate a lower limit for the 15–37 GHz spectral index. The spectral index lower limits are around 4–5. Considering that SSA cannot account for a spectral slope more inverted than 2.5, these values indicate that an additional absorption mechanism, such as FFA, which can lead to very inverted slopes (Rodriguez et al. 1993; Mhaskey, Paul & Krishna 2021), might be in play. However, considering the short time-scales of our sources and the fact that these data are not simultaneous, also temporal variability can contribute to the inferred spectral indices.

Despite frequent detections at 37 GHz, and some at 15 GHz, all sources were in the low state in the JVLA observations. However, considering the low-to-moderate detectabilities (1.5 per cent–25 per cent) and the short time-scales of the sources at 37 GHz, it is

not infeasible that none of them were flaring at the time of the two epochs of the JVLA observations.

In the following, we discuss different phenomena that are able to cause variability in AGN. It should be kept in mind that the physical explanation for the observed variability might not be the same in all sources or that it can be a combination of more than one mechanism. For completeness, we include a number of explanations that we have been able to reject or that are unlikely to be responsible for the extreme behaviour. Since not much can be said regarding the sources that have very few detections only in some of the bands, the discussion mostly considers the sources with the most complete data, that is, J1228+5017, J1232+4957, J1522+3934, and J1641+3454.

5.1 Rejected explanations

More data, especially multifrequency monitoring of the flares, are absolutely necessary to narrow down the possible explanations, however, based on the current data some scenarios can already be ruled out. These alternatives cannot be solely responsible for the observed properties of our sources, but we cannot definitely exclude their presence either.

5.1.1 Normal relativistic jets

Based on the results in this paper and in Berton et al. (2020b), it is obvious that the sources in our sample do not host persistent, continuously visible relativistic jets similar to those seen in other jetted NLS1s or any other class of jetted AGN. Several jetted NLS1s exhibit 37 GHz behaviour similar to the sources studied in this paper (Lähteenmäki et al. 2017), and all of them also show core or core-jet structures in mas-scale VLBI observations (e.g. Doi, Asada & Nagai 2011; Richards et al. 2015; Lister et al. 2016). In general, the VLBI flux densities of the previously studied jetted NLS1s vary from a few mJy to hundreds of mJy and thus are at a level that should have been easily detectable in our VLBA observations. However, the non-detections of these sources either imply that the radio core is very faint, $< 0.5\text{ mJy}$, or possibly absorbed (see Sections 5.2.4 and 5.3.2).

We did not expect to be able to resolve the possible jet with the JVLA – except perhaps in the highest frequency bands – since the flaring behaviour implies that we see these sources at quite small angles. However, our initial assumption, again based on the observations of other jetted NLS1s, was that these sources would show flat or inverted spectra toward higher frequencies. Only one of our sources, J1228+5017, shows a radio spectrum that can be deemed flat, and none of the detected sources show any hints of an inverted spectrum in the JVLA observations. Regarding the non-detected sources, from these results, we can only infer that their spectra do not turn inverted toward higher frequencies.

With these combined results we are able to reliably rule out the possibility that the variability in our sources is due to flares in a relativistic jet similar to those in other jetted NLS1s or AGN. This does not necessarily mean that the jet is absent, but in the low state, it seems to be undetectable, implying that there must also be other contributors to the observed behaviour.

5.1.2 Kinematically young jets

These results also rule out one of our early hypotheses, which was that these sources would be kinematically young and have considerably high radio spectrum turnover frequencies due to that (O’Dea & Saikia 2021). The 37 GHz behaviour could be explained as radio

flares superimposed on a convex radio spectrum of a peaked source (Tornikoski et al. 2001, 2009; Tornainen et al. 2005). Obviously this is not the case, as we do not see any signs of spectra resembling those of peaked sources. Also the long-term temporal behaviour disagrees with this scenario since several of these sources have been detectable at 37 GHz at the same flux density level for the past ~ 10 yr, ever since the observations first started. In the case of a kinematically young source, the turnover frequency is expected to decrease very fast during the early stages of its life, staying above > 40 GHz only for 6–20 yr (Berton et al. 2020b) – the kind of evolution we should be able to recognize at 37 GHz, and also at 15 GHz, as increasing or decreasing detectability, or as long-term permanent changes in the flux density levels. There are a few sources that have not been detected during the past few years even when they have been observed regularly (J1232+4957 and J1510+5547), which indicates temporal changes in these sources. Even in these cases kinematically young jets seem improbable since the evolution is not so fast that we would not have been able to detect a convex spectrum at lower frequencies with the JVLA. It should be noted that whereas kinematically young jets with SSA cannot explain the behaviour of our sources, it does not mean that the jets in these sources could not be young.

5.1.3 Fast radio bursts

The seemingly sporadic detectability, implying very short time-scales, raised the question of whether this phenomenon could be related to fast radio bursts (FRB). FRBs are short, subsecond duration broad-band Jy-level pulses of extragalactic origin (for a recent review, see Petroff, Hessels & Lorimer 2022). Several repeating FRBs have been found, and in principle, they could fall into the MRO beam during an observation. In practice, it is very unlikely that such an event could account for the detections of these sources: first, the moderately long 1600–1800 s integration time used at MRO would average out even a Jy-level, subsecond pulse to an undetectable level, and second, FRBs have very steep spectra with an average spectral index of -1.5 (Macquart et al. 2019), making them fainter and even harder to detect at high radio frequencies.

5.1.4 Tidal disruption events

TDEs occur when a star passes by too close to a supermassive black hole and gets disintegrated. In some extreme cases, these events can result in the launching of (mildly) relativistic jets, reaching luminosities around 10^{42} erg s $^{-1}$, and therefore possibly bright enough to explain our 37 GHz detections (Alexander et al. 2020, and references therein). However, the time-scales of TDEs are in the range of tens to hundreds of days and thus not compatible with the behaviour of our sources. Furthermore, so far a TDE has never been observed twice in the same source, and thus it seems extremely improbable that repeated detections over 10 yr could be due to TDEs. There are some records of partial TDEs (Campana et al. 2015) when the whole star does not get destroyed but continues to orbit the black hole, causing small TDEs once per orbit. Whereas partial TDEs could be responsible for repeated radio flares, they are unlikely to produce variability at a time-scale of days.

5.2 Unlikely explanations

In the following, we discuss some alternatives that are unlikely, but cannot be totally ruled out yet, or are not able to explain our sources on their own, but might contribute to the observed properties.

5.2.1 Observational effects

Interestingly, it seems that in all cases an inverted spectrum or a high state is seen only in single-dish observations, whereas interferometric observations show a barely flat or a steep spectrum, if the source is detected at all. This raises the question of whether the difference could be explained by contamination by nearby compact sources that the larger beams of the single-dish telescopes pick up, or by emission resolved out with radio arrays. The first explanation – different beam sizes – can be ruled out since based on the JVLA images mapping the OVRO beam there are no other strong radio sources close to any of our targets, and thus even the largest beams (MRO and OVRO) should not suffer from confusion.

On the other hand, resolved-out emission can contribute to the discrepancy, but not explain all of it. In A-configuration, the largest angular scales that the JVLA can see are approximately 5.3, 3.6, 2.4, 1.6, and 1.2 arcsec in X , Ku , K , Ka , and Q bands, respectively. In the worst-case scenario, the lowest- z source in Q band, this translates to 1.70 kpc. Considering the light traveltimes argument, it is obvious that emission at these scales cannot explain the variability time-scales seen in our sources. There can be a contribution from the resolved-out emission, but, for example, at 37 GHz based on the MRO detection threshold, it cannot exceed ~ 200 –300 mJy, otherwise, we would be able to detect these sources much more frequently. Similarly, OVRO, with a beam of the same size as MRO, gives an upper limit of ~ 10 mJy for the 15 GHz resolved-out emission. Since there are no emission sources at kpc-scale that can produce such an inverted spectrum between 15 and 37 GHz, it is reasonable to assume that the real 37 GHz flux density is at a similar or lower level than the 15 GHz flux density, suggesting that extreme variability is still present.

In addition, based on the preliminary results of our JVLA monitoring campaign of J1522+3934 using the B-configuration in X and K bands (VLA/23A-061, PI: Berton), the beam size does not have a significant impact on the flux density. In the B-configuration, the beam is about three times larger than in the A-configuration in both bands and also the largest detectable angular scales – 17 arcsec in X and 7.9 arcsec in K , 24.1 and 11.2 kpc at the redshift of J1522+3934, respectively – are significantly more extended than in A-configuration. However, the observed flux densities in A- and B-configurations are the same within the errors, further supporting that any resolved-out emission is not able to explain the difference.

5.2.2 Precessing jet

One alternative to explain variability in AGN is the precession in the jets (e.g. Kudryavtseva et al. 2011), leading to changes in the viewing angle and thus in the strength of relativistic boosting. Precession can be caused by a tilted accretion disc via different mechanisms, such as the radiation-driven warping instability (Pringle 1996) or the Bardeen–Petterson effect (Bardeen & Petterson 1975) due to Lense–Thirring precession (Thirring 1918). Precession can also be observed in binary supermassive black hole systems (Begelman, Blandford & Rees 1980). However, in all these cases the expected, and so far observed, precession period is of the order of years (e.g. Kudryavtseva et al. 2011; Liska et al. 2018; Horton et al. 2020), rather than days as in our case. It is therefore unlikely that precession on its own could explain the properties of these sources.

5.2.3 Intermittent activity

The lack of detectable jets in these NLS1s might indicate a kinematically young age – that was already discussed in Section 5.1.2 – or

intermittent activity. Intermittent activity due to radiation pressure instabilities in the accretion disc was evoked to explain the excessive number of kinematically young radio AGN, such as gigahertz peaked sources (GPS), and especially their subclass of compact symmetric objects (Czerny et al. 2009). For a black hole with a mass of $10^8 M_\odot$, the duration of the activity phases is estimated to be 10^3 – 10^4 yr, and the breaks between them 10^4 – 10^6 yr. For lower black hole mass sources, such as NLS1s, these time-scales are shorter, but certainly not short enough to explain the variability we are observing.

Also 3D GRMHD simulations have yielded similar results; Lalakos et al. (2022) find that before establishing stable, powerful relativistic jets an AGN can go through several cycles of intermittent activity, with the jets turning on and off and drastically changing direction. This leads to an X-shaped radio morphology seen in 5 per cent–10 per cent of radio galaxies, and, naturally, considerable variability. Using the results in Lalakos et al. (2022), we can estimate that the launch-to-quench time-scale for a black hole with a mass of $10^7 M_\odot$ is 10–100 yr, and the jets re-emerge after 100–1000 yr. The time-scale is too long for our sources, but it suggests that in lower black hole mass AGN we could be able to follow, at human time-scales, the chain of events from the initial launch of the jets until they are quenched by the infalling gas. As low black hole mass jetted sources NLS1s could be an optimal target for these kind of studies.

Shorter time-scale intermittency can manifest itself as a result of changing injection rate of plasma into the jet base/jet (e.g. Lohfink et al. 2013; Fedorova & Del Popolo 2023). Between these events the jet can be totally absent or very weak, possibly explaining the low state of our sources. What remains unclear is whether this kind of events can account for the required short time-scales and high variability amplitudes, and how these events manifest themselves in the radio regime. The classical viscous and thermal time-scales associated with an accretion disc around a black hole with a mass of $\sim 10^7 M_\odot$ are too long to explain the variability, whereas the magnetic time-scale dominating the inner parts of the disc can be considerably shorter (Livio, Pringle & King 2003; King et al. 2004). The magnetic time-scale is the time on which the poloidal magnetic fields in different parts of the disc can spontaneously align, possibly changing the dissipation in the disc and its coupling to the jet. Local changes in the magnetic field alignment can cause small-amplitude flickering at very short time-scales, whereas large-amplitude events, where the magnetic field is aligned in a considerable fraction of the disc, are rarer. Thus this kind of intermittency could possibly explain either the short time-scales or the high amplitudes, but not both.

It is worth noting that even if intermittent activity would not be the culprit in this case, we do see signs of that among these sources. Assuming that we are now observing the jets in our sources at small angles as indicated by the variability, it is evident from the misalignment between the radio emission and the host galaxy in fig. 5, panel (c) in Järvelä et al. (2021) that J1522+3934 has experienced an earlier activity period. However, the projected size of the structure is almost 20 kpc, well beyond the host galaxy, implying that the activity period has been longer than what would be expected in the aforementioned scenarios. Based on the current data, we also cannot determine whether the jets turned off or just changed direction.

5.2.4 Pure FFA

A possible way to explain the flares is to assume that the underlying radio emission of the relativistic jet is totally free–free absorbed by ionized gas in the low state, and would only occasionally break through the absorbing screen due to intrinsic flaring, or due to very

fast drops in the absorption (see Section 5.3.2). By solving the transfer equation, it is possible to prove that such a scenario is not impossible, as it does not require an unreasonable amount of gas. Let us assume that the radiation produced by the jet is free–free absorbed as follows:

$$I_\nu = I_{\nu,0} e^{-\tau_\nu} \quad [\text{erg s}^{-1}], \quad (7)$$

where τ_ν is the optical depth, $I_{\nu,0}$ is the radiation produced by the jet, and I_ν is the radiation we observe after it has crossed the ionized gas. For simplicity, let us do our calculation at 10 GHz, and assume that the jet emission is not detected. The detection threshold of the JVLA for our observations in the X band is 10 μJy , so we can assume an upper limit for the observed flux density of 30 μJy . Let us also assume that the jet has an underlying flat spectrum and that the unabsorbed flux density at 10 GHz is 1 Jy. Using the previous equation, we can obtain an optical depth $\tau_\nu \sim 10$. The optical depth of the ionized gas cloud depends on the absorption coefficient k_v^{ff} , following

$$\tau_\nu = \int_0^l k_v^{\text{ff}} dr, \quad (8)$$

where l is the size of the absorbing cloud. The FFA coefficient is

$$k_v^{\text{ff}} \simeq 3.69 \times 10^8 Z^2 \frac{N_e N_i}{\sqrt{T_e}} \frac{1}{\nu^3} g_{\text{ff}} \quad [\text{cm}^{-1}], \quad (9)$$

where N_e is the electron number density, N_i is the number density of the ions, T_e the electron temperature, Z the atomic number, and g_{ff} is the Gaunt factor. Assuming hydrogen gas ($N_e = N_i$), and using the approximation of the Gaunt factor between 0.3 and 30 GHz, the coefficient becomes

$$k_v^{\text{ff}} \simeq 0.21 N_e^2 T_e^{-1.35} \nu^{-2.1} \quad [\text{cm}^{-1}]. \quad (10)$$

If we integrate this assuming that the cloud has a uniform density and temperature, the optical depth becomes

$$\tau_v^{\text{ff}} \simeq 0.0824 T_e^{-1.35} \nu^{-2.1} N_e^2 l. \quad (11)$$

Inverting this equation, we can derive

$$l \simeq \frac{\tau_v^{\text{ff}}}{0.0824 N_e^2} T_e^{1.35} \nu^{2.1} \quad [\text{pc}]. \quad (12)$$

Since we now know that $\tau_v^{\text{ff}} \sim 10$, we can try to calculate the size of the absorbing clouds by assuming different values of electron density and temperature, at the frequency of 10 GHz. For $N_e = 10^4 \text{ cm}^{-3}$ and $T_e = 10^4 \text{ K}$, which are rather typical values, we obtain $l = 38 \text{ pc}$. For a higher density, possibly similar to the conditions of a shock, of $N_e = 10^5 \text{ cm}^{-3}$ and $T_e = 10^5 \text{ K}$, the size decreases to $l = 8.6 \text{ pc}$. Such size is comparable to that of the Orion Nebula. Finally, if $N_e = 10^5 \text{ cm}^{-3}$ and $T_e = 10^4 \text{ K}$, the resulting $l = 0.38 \text{ pc}$, which is too small for a star-forming region, but may be closer to the expectations of a region of gas ionized via shock by the jet itself. Due to the $\nu^{2.1}$ dependence, the required size of the ionized cloud increases at higher frequencies. For example, at 50 GHz it would need to be ~ 30 times larger to effectively absorb all the emission. This would imply sizes of hundreds of parsecs, unlikely ionized by the AGN, but of a characteristic size for a star-forming region (e.g. Congiu et al. 2023). Lower densities and temperatures instead require unreasonably large sizes. For instance, $N_e = 10^3 \text{ cm}^{-3}$ and $T_e = 10^4 \text{ K}$ lead to $l = 3.8 \text{ kpc}$, which is not realistic since this requires a uniform distribution of ionized gas as large as a small galaxy.

Even if the previous considerations show that this scenario is feasible, there are some issues that we cannot ignore. First of all, in this scenario in the low state, the jet emission needs to be totally absorbed – otherwise, we would see an inverted spectrum – thus the

JVLA radio emission needs to originate outside the absorbed region. Were the absorption due to a star-forming region, it could as well be the source of the faint low-state radio emission. As the star-forming region cannot explain the variability, it would have to be intrinsic to the jet that would occasionally get bright enough to break through the FFA screen. However, assuming that the underlying relativistic jet is similar to those in other jetted NLS1s, we would assume the time-scales to be comparable too, which is not the case.

Another way of producing the observed flares is by means of a variable optical depth, which in turn requires either fast-moving clouds (see Section 5.3.2) or a rapid propagation of the jet throughout an interstellar medium with variable density and temperature (Wagner, Bicknell & Umemura 2012; Kino et al. 2021).

5.2.5 Geometrical effects

The changes in the Doppler factor due to circumstances internal or external to the jet have been evoked to explain large-amplitude flares in AGN. Such circumstances could be the result of changes in the orientation of the jet, or parts of it, or due to the jet substructure, such as a helical magnetic field (Villata & Raiteri 1999; Mignone et al. 2010; Raiteri et al. 2017, 2021). This variability is characterized by achromatic frequency behaviour in the affected bands.

For example, an FSRQ CTA 102 has shown in the optical a somewhat similar behaviour to what we see in our sources in radio (Raiteri et al. 2017). The source increased its optical magnitude by six magnitudes, but in comparison the other frequencies were almost unaffected by the flare. In our case, the flare seems to predominantly affect the radio emission and not other wavelengths (Romano et al. 2023). Raiteri et al. (2017) suggested that the variability in CTA 102 was caused by changes in the viewing angle due to peculiar jet geometry. If this is the case, we are observing different regions of the jet at different angles. In our sources only the radio emission would be seen at a small viewing angle, experiencing stronger relativistic boosting due to the higher Doppler factor. This scenario could be consistent with what is seen in several simulations. Jets propagating in dense ISM cannot proceed in a straight line but tend to wiggle around the least resistance path (Wagner et al. 2012).

To estimate the feasibility of this scenario, we can estimate the level of change in the Doppler factor required to explain the extreme variability we observe in our sources. We assume the unbeamed flux density, S_0 , to be at the level of the JVLA values, and the beamed, S_{obs} , to be close to the MRO detections. The emission is boosted as:

$$S_{\text{obs}} = S_0 \delta^p, \quad (13)$$

where $p = 2 - \alpha$ for a continuous jet stream, and $p = 3 - \alpha$ for a transient emission region, such as a blob or a knot in the jet. We assume the jet spectral index to be $\alpha = 0$. A few different cases of the unbeamed and beamed flux densities are shown in Table 9. The Doppler factors in case of a continuous stream are very high, but more reasonable in the case of a transient emission region in the jet. We calculated the required change in the viewing angle resulting in the estimated changes in the Doppler factor (Table 9). We did the calculation with two different Lorentz factors (Γ) characteristic for jetted NLS1s: 10 and 20 (Abdo et al. 2009). In case of the continuous stream, when $p = 2$, $\Gamma = 10$ is not high enough to reach the Doppler factors shown in Table 9, and even $\Gamma = 20$ yields results only in case of $\delta = 50$ ($\Delta\theta = 18^\circ$), thus we list the viewing angle changes only for the $p = 3$ case. The required changes are not unreasonable, for example, in Raiteri et al. (2017) the viewing angle change is $\sim 9^\circ$. However, in their case, the time-scale of the change is of the order

of several weeks, whereas in our case it is of the order of days. Also other issues remain, as discussed below.

This hypothesis requires a relativistic jet to be present, but we do not see any clear signs of this in any of our sources. In the first-order approximation, in this scenario either the jet needs to change direction and consequently its Doppler factor, or new components, possibly with higher Lorentz factors, would need to be ejected. Also other factors, for example, temporal variability in the physical conditions of the jet – such as the magnetic field, and the density and energy distribution of the relativistic particles – may contribute, but their impact can be expected to be less significant.

If the changes are due to the re-orientation of some parts of the jet it is hard to explain why we observe the flaring behaviour only in radio. This might require the same part of the jet to consistently change its orientation, which does not seem likely. In this case, the variability should be achromatic, which is something we cannot yet study with the current data. If the flares are due to new components ejected, we would expect to see the underlying jet also when it is not flaring, since it should be relativistically boosted also between flares unless the blobs have considerably higher Doppler factors than the continuous stream. In both these scenarios, the emission comes from the whole jet and therefore requires the emitting region to be very close, within the innermost parsec, to the black hole, to be able to match the estimated time-scales. An alternative way of producing drastic changes in the Doppler factor only in some parts of the jet is magnetic reconnection, which will be discussed in Section 5.3.3.

Another geometrical effect in relativistic jets that causes changes in the observed flux density is due to large-scale, ordered helical magnetic fields. If the jet is magnetically dominated, the magnetic field can drive helical streams within the jet. These streams can experience differential Doppler boosting along the jet when on one side of the helix the radiation gets relativistically boosted and on the other side it gets diminished (Steffen 1997; Clausen-Brown, Lyutikov & Kharb 2011; Gabuzda 2018).

In case of a continuous stream we should be able to see the jet at all times, which is not the case, so we can assume that in this scenario the flares are caused by a blob moving in the jet, thus $p = 3$ in equation (13). For simplicity and to maximize the strength of the effect, let us assume a helical magnetic field seen exactly at the helix angle. Assuming constant β the changes in the flux density only depend on the Doppler factor whose value depends on the angle between the helical stream within the jet and the line of sight as:

$$\delta = \frac{\sqrt{1 - \beta^2}}{1 - \beta \cos\theta}, \quad (14)$$

where $\beta = v/c$, and θ is the angle compared to the line of sight. In our scenario, θ has a minimum of 0° . Let us estimate the radius of the jet in case of the longest e -folding time-scale in an MRO-detected flare from Table 8; the 2017 decaying flare of J1509+6137. The flux density decreased from 970 to 610 mJy in 5.97 d in our reference frame, thus in $5.97 \text{ d} \times \delta$ in the source frame. Based on Table 3 let us assume that $S_0 = 0.1 \text{ mJy}$, and that $S_{\text{obs},\text{max}} = 970 \text{ mJy}$, which happens when $\theta = 0^\circ$. Using equation (13), we can estimate that the required Doppler factor at the maximum flux density is $\delta_{\text{max}} = 21.3$, and at $S = 610 \text{ mJy}$ it is $\delta_{610 \text{ mJy}} = 18.3$. Using equation (14) with $\delta_{\text{max}} = 21.3$ and $\theta = 0^\circ$, we get $\beta = 0.996$. Assuming β stays constant, and using $\delta_{610 \text{ mJy}} = 18.3$, we can solve for $\theta_{610 \text{ mJy}} = 2.41^\circ$. The radius of the jet can be solved from

$$R = \frac{b}{2\pi} \frac{360^\circ}{2.41^\circ} [\text{m}], \quad (15)$$

where R is the radius of the jet, and b is the distance the blob has travelled along the arc of the outer edge of the jet. In this case $b = 5.97 d \times \delta_{\max} \times 0.996 c = 3.28 \times 10^{15} \text{ m}$, and $R = 7.80 \times 10^{16} \text{ m} = 2.53 \text{ pc}$. This is the least extreme case, and in other flares where the changes were faster also the radius of the jet would have to be smaller to account for the variability. In cases when $\theta_{\min} \neq 0$, β would have to be larger to result in the same δ , and R would have to be smaller than in the $\theta_{\min} = 0$ case.

Based on other AGN, jet diameters of a few parsecs are measured at projected distances from ~ 1 to 10 pc from the AGN core (Kovalev et al. 2020), and thus most likely outside the BLR. This brings us to the same question again: where is the jet when it is not flaring? Though it should be noted that we estimated the radius assuming the most favourable conditions for Doppler factor changes, thus it is likely that in reality the radii should be smaller, but by how much is unclear.

5.2.6 Lensing and scattering

Micro- and millilensing and scattering, especially extreme scattering events (ESE), can cause considerable variability in light curves of extragalactic sources. First identified in the 1980s (Fiedler et al. 1987), ESE cause radical variability in the flux densities of radio sources due to intervening plasma lenses in the ISM (Bannister et al. 2016a) of our Galaxy. Radio flux density variability close to an order of magnitude has been attributed to ESEs (Bannister et al. 2016b), whereas their multiwavelength behaviour is unknown. The ESEs observed so far have not shown amplitude variability comparable to what we see in our sources, and their characteristic time-scales are of weeks to months, and thus longer than the variability we detect in these NLS1s, although tentative ESEs with time-scales of days have been detected (Cimò et al. 2002; Bannister et al. 2016a). Most ESEs are identified at radio frequencies of a few GHz since the refractive power of the plasma lens depends on the wavelength and thus the phenomenon gets stronger toward longer wavelengths. Although, clearly identifiable ESEs have been observed at a frequency as high as 15 GHz (Kara et al. 2012; Pushkarev et al. 2013). However, in our case, the 37 GHz flux densities are significantly higher than the 15 GHz values, arguing against a possible ESE origin of the variability. Last, considering how rare ESEs are it is unlikely that we would witness this frequent ESE activity in a few sources, especially residing this far from the Galactic plane.

Microlensing by stellar mass objects ($< 10^2 M_{\odot}$) or millilensing by objects with masses around 10^2 – $10^6 M_{\odot}$ have been shown to cause variability in AGN light curves. In this scenario, the lensing mass lies either in the same galaxy as the AGN or between the AGN and the observer, and the time-scales of this variability can span from hours to years, depending on the size of the lens (Vedantham et al. 2017; Król et al. 2023). Unlike ESEs, this variability is achromatic at least up to hundreds of GHz and thus the amplified flux density only depends on the intrinsic brightness of the source at a given frequency. In the radio regime, this phenomenon has been labelled as symmetric achromatic variability and has been detected in several sources, some of them repeating (Vedantham et al. 2017; Peirson et al. 2022). In the AGN lensing events so far, the maximum amplification of the flux density is around an order of magnitude. Even if in the case of a binary lens in the microlensing regime, we could expect to observe fast, repeating variability, the question of the feasibility of the required extreme amplitude amplification remains. It has been analytically shown that under favourable conditions, that is, when the source lies relatively close to a compact lens and at a small angular

distance from the caustic line, such extreme amplitude amplification can take place (Bakala et al. 2023). However, reaching these exact conditions in seven out of 66 sources seems quite unlikely, so whereas this alternative is not unphysical it might be improbable, at least as an explanation for all sources.

5.3 Viable explanations

5.3.1 Jet–cloud/star interaction

Shocks in the interaction region of a jet and ISM can efficiently accelerate the electrons and thus increase the observed flux density of the jet (e.g. Fraix-Burnet 1992). In the case that the ISM consists of clumpy clouds only, parts of the jet might come in contact with them resulting in regions of enhanced emission that are smaller than the radius of the jet (Gómez et al. 2000). Particularly relevant in our case is the possible interaction between the jet base and BLR clouds or stars (Araudo, Bosch-Ramon & Romero 2010; Bosch-Ramon, Perucho & Barkov 2012; del Palacio, Bosch-Ramon & Romero 2019). Using reasonable physical parameters for the BLR clouds, del Palacio et al. (2019) found a high duty cycle (10–100) for jet–cloud interactions, indicating that at any given time the jet should be interacting with several clouds. Of course, in case no extended jet is present this duty cycle is lower. The number of interactions with stars depends greatly on the size of the jet (Araudo, Bosch-Ramon & Romero 2013). However, considering that new TDEs are frequently discovered these days the number of stars very close to the central black hole is not negligible. According to simulations, the time-scales of these events are of the same order as the estimated time-scales of our sources, that is, from less than a day to a few days, and they can considerably increase the luminosity of the source. Whereas the time-scales fit our observations, a BLR cloud or a massive star entering the jet is expected to produce a flare that should be observable over the whole electromagnetic spectrum, which is behaviour not consistently observed in our sources. On the other hand, based on *Fermi* data, there does not seem to be strong evidence pointing at the BLR photons interacting with the jet since most blazars do not show the expected high-energy cut-off (Costamante et al. 2018). However, this result can be explained if the main gamma-ray-emitting region in AGN is outside the BLR and swamps the gamma-ray emission originating inside the BLR. As a result, jet–cloud/star interaction can still cause flares observable in lower energies, for example, in the optical and radio regimes (Romero, Cellone & Combi 2000; Romero et al. 2002).

The issue of the missing jet also remains with this explanation. Although if the jet is small and embedded in the BLR clouds, also FFA could play a role in this scenario. Furthermore, since no dedicated simulations exist, it is unclear what the temporal evolution of these flares in radio is. More detailed simulations will be required to estimate if this hypothesis could provide a feasible explanation for the extreme variability of our sources.

5.3.2 Relativistic jet and FFA with moving clouds

In this scenario, the starting point is similar to that in Section 5.2.4, but the region of ionized gas is not uniform and stationary but consists of moving ionized gas clouds. The AGN would be totally free-free absorbed most of the time and the flares take place when the nucleus is temporarily revealed. In other words, the behaviour we observe would be caused by a combination of obscuration and geometry, and not by an intrinsic change in the jet activity. Some support for this hypothesis was found in J1641+3454 in which no absorption was detected in X-rays just after a flare when the nucleus probably was

exposed, but a possible warm absorber is seen in the X-ray spectrum when the source is in a low state (Lähteenmäki et al. in preparation). In this scenario, the time-scale only depends on the size of the gap in the clouds, its distance from the radio-emitting source, and its orbital velocity, so the time-scales can be arbitrarily short.

In this hypothesis, the covering medium would most likely be ionized BLR clouds that are considerably denser and smaller than ISM clouds. The BLR clouds can be as dense as $N_e = 10^{11} \text{ cm}^{-3}$ (Ferland et al. 1992) with sizes around 100–400 solar radii and thus easily able to absorb bright radio emission even at high frequencies. The covering factor of the BLR in optical is believed to be around 10 per cent–50 per cent, but reaching ~ 100 per cent towards certain directions (Gaskell 2009).

However, open questions remain also in this case. This scenario requires that the jets of these sources are kinematically very young and still within the BLR, and also that their advancement is hindered enough by the BLR so that they have stayed within the BLR our whole observing period, about 10 yr. Assuming a BLR outer radius of 0.1 pc, the jet propagation speed would have to be $\lesssim 0.03 \text{ c}$ for this hypothesis to be viable. Wagner et al. (2012) report a jet propagation speed of 0.003–0.16 c in the presence of clouds impeding its progress. Thus a slow jet could stay within the BLR for up to a hundred years, easily enough for our case (Kino et al. 2021; Savolainen et al. 2023).

5.3.3 Magnetic reconnection

Magnetic reconnection in the jet or in the black hole magnetosphere has been evoked to explain fast variability in AGN, especially at GeV and TeV energies (e.g. de Gouveia Dal Pino, Piovezan & Kadovski 2010; Giannios 2013; Kadovski, de Gouveia Dal Pino & Singh 2015; Shukla & Mannheim 2020). It can account for high-amplitude variability at time-scales from minutes to days. If magnetic reconnection were to take place in the jet in the form of so-called jets-in-jets or minijets (e.g. Ghisellini & Tavecchio 2008; Giannios, Uzdensky & Begelman 2009; Nalewajko et al. 2011), the jet would need to be heavily absorbed, since it remains undetected, and it would likely still be within the BLR. Proof of classic gamma-ray flares happening inside the BLR does exist (Vovk & Neronov 2013; Liao & Bai 2015), and also signs of gamma-ray pair attenuation have been found (Poutanen & Stern 2010), further suggesting that flares can happen inside the BLR. However, the research so far has concentrated on the high-energy characteristics of minijets, and the production of radio emission and flares in the context of magnetic reconnection in the jet has not been studied, thus it is unclear whether this scenario could result in the behaviour we see in our NLS1s.

An alternative for the magnetic reconnection in the jet is the magnetic reconnection in the black hole magnetosphere (e.g. de Gouveia Dal Pino et al. 2010; Kadovski et al. 2015; Kimura et al. 2022; Ripperda et al. 2022). The advantage of this explanation is that it does not require the presence of a permanent relativistic jet. The emission characteristics of these kinds of events have been studied utilizing GRMHD simulations (Ripperda et al. 2022) and also development of the theoretical framework has been started (Kimura et al. 2022), but we still lack any direct evidence of this. de Gouveia Dal Pino et al. (2010) and Kadovski et al. (2015) argue that the radio and gamma-ray emission in low-luminosity AGN can be explained with magnetic reconnection in the black hole magnetosphere, whereas blazars also require a significant contribution from the relativistic jet. Based on their model, an effectively accreting black hole with a mass of 10^7 M_\odot and turbulence-induced fast reconnection can show magnetic reconnection power spanning from 10^{39} to $10^{43} \text{ erg s}^{-1}$ and thus likely enough to explain the flares in our sources.

5.4 Implications

It is evident that more data, especially simultaneous multifrequency observations of the flaring state, are required to determine the origin of the extreme variability seen in these NLS1s. Already based on the current data, the most common causes of radio variability in AGN can be ruled out, or they would require considerable fine-tuning. The strictest requirements come from the variability time-scales, especially coupled with the extremely high, 3–4 orders of magnitude, amplitude of the variability. The time-scales are extraordinarily short and therefore require a compact, milliparsec-scale, emitting region, or, alternatively, a peculiar interplay between the jet and the BLR clouds. Whereas intrinsic variability mechanisms allowing very short time-scales and high amplitudes exist, most of them are still very little studied or only based on simulations or theoretical work, and lack observational evidence. To determine if any of them could explain the behaviour of our sources, a more detailed theoretical framework, possibly dedicated simulations, and especially targeted observations will be needed. It should be kept in mind that we cannot exclude the possibility that we are seeing a new type of variability either. Either way, catching flares in these sources will be challenging due to the short time-scales and sporadic activity, but considering that these NLS1s exhibit one of the most extreme radio variability seen in AGN so far, they do deserve our full attention.

One of the most interesting aspects of the discovery of these sources is that they were found among two very differently selected samples whose final detection percentage at MRO turned out to be very high at 12 per cent – eight sources out of 66 were detected. Whether our selection criteria actually helped us select NLS1s exhibiting this behaviour or if it was pure coincidence remains unclear. Observations of other NLS1 samples selected using similar and different selection criteria will be needed to estimate the impact of the selection effects.

Either way, detecting > 10 per cent of a presumably mostly radio-silent NLS1 sample is extraordinary and raises the question of whether this variability phenomenon is characteristic of NLS1s or possibly early-stage AGN, or if similar sources are hiding also among radio-weak AGN of other classes. For obvious reasons, radio-weak AGN have not been a target of extensive high radio frequency monitoring campaigns and we therefore know very little about their behaviour in that regime. It is possible that also strong radio AGN exhibit this kind of behaviour, but that it is swamped by other sources of radio emission and thus has remained undetected. Investigating in which kind of sources this phenomenon can be seen can help us to determine the cause of the variability. Being able to identify any common properties these sources have will also help us to find more of them.

Whether this kind of variability is limited to early-stage AGN or if it is a more common phenomenon has implications for our current understanding of AGN. These sources clearly represent an unknown population of AGN, that has gone unnoticed so far. If they are a new type of jetted AGN or something else entirely, is unclear, as is their evolution and relation to other classes of AGN. Furthermore, we do not know how common they are or if they are characteristic to the local Universe, or also exist at higher redshifts. Further studies are also required to estimate which kind of a role they play in AGN feedback over the cosmic time.

6 CONCLUSIONS

In this paper, we investigated the origin of the extreme radio variability seen in seven NLS1s using the JVLA, the VLBA, MRO, and OVRO observations. These extraordinary sources defy an easy

explanation, but the new data presented in this paper allowed us to rule out some alternatives and set additional constraints on the possible explanations. Our main conclusions are:

(i) The behaviour of these sources is hard to explain with the usual variability mechanisms in AGN – instead a more complex scenario or possibly a new type of physical mechanism to produce variability is required.

(ii) The amplitude of the variability – 3–4 orders of magnitude – seen in these sources is unprecedented, but it remains unclear whether it is intrinsic to the source, or caused by some external circumstances.

(iii) The variability time-scales indicate that if the variability is intrinsic the emitting region needs to be milliparsec in size. This implies that the emission originates close to the black hole, clearly inside the BLR, or from limited, confined regions in the jet.

(iv) The high detection percentage among the original sample, which were not expected to be strong radio emitters, implies that these kinds of sources could be quite common, but so far our understanding of this new population of AGN is very limited.

Revealing the nature of these peculiar sources is of utmost importance as they might be the first representatives of a new type of AGN variability, and/or a new class of jetted AGN entirely. In the future, an increase in the sample size will be essential to explore this new population. Their short time-scales and sporadic activity pose an observational challenge, also given how diverse their behaviour is at different frequencies. High-cadence multifrequency radio monitoring with an instrument sensitive enough to detect also the rising and decaying parts of the flares will be essential to better characterize their variability and set additional constraints to the different hypotheses concerning these sources. Furthermore, given the small spatial scales implied by the variability time-scales, many of the upcoming telescopes and instruments currently under development, such as the next generation VLA in radio, the Multi-Conjugated Adaptive Optics Assisted Visible Imager and Spectrograph, and the High Angular Resolution Monolithic Optical and Near-infrared Integral field spectrograph in the optical/near-infrared, and *Athena* in X-rays, will be crucial to study the spatial properties and evolution of these remarkable sources.

ACKNOWLEDGEMENTS

The University of Oklahoma Land Acknowledgement Statement:

Long before the University of Oklahoma was established, the land on which the university now resides was the traditional home of the ‘Hasinais’ Caddo Nation and ‘Kirikiris’ Wichita & Affiliated Tribes. This land was also once part of the Muscogee Creek and Seminole nations.

We acknowledge this territory once also served as a hunting ground, trade exchange point, and migration route for the Apache, Comanche, Kiowa, and Osage nations. Today, 39 federally recognized tribal nations dwell in what is now the State of Oklahoma as a result of settler colonial policies designed to assimilate Indigenous peoples.

The University of Oklahoma recognizes the historical connection our university has with its Indigenous community. We acknowledge, honour, and respect the diverse Indigenous peoples connected to this land. We fully recognize, support, and advocate for the sovereign rights of all of Oklahoma’s 39 tribal nations.

This acknowledgment is aligned with our university’s core value of creating a diverse and inclusive community. It is our institutional

responsibility to recognize and acknowledge the people, culture, and history that make up our entire OU Community.

This publication makes use of data obtained at Metsähovi Radio Observatory, operated by Aalto University in Finland.

The National Radio Astronomy Observatory is a facility of the National Science Foundation operated under cooperative agreement by Associated Universities, Inc. CIRADA is funded by a grant from the Canada Foundation for Innovation 2017 Innovation Fund (project 35999), as well as by the Provinces of Ontario, British Columbia, Alberta, Manitoba and Quebec.

This research has made use of data from the OVRO 40-m monitoring program (Richards et al. 2011), supported by private funding from the California Institute of Technology and the Max Planck Institute for Radio Astronomy, and by NASA grants NNX08AW31G, NNX11A043G, and NNX14AQ89G and NSF grants AST-0808050 and AST-1109911.

This research has made use of the NASA/IPAC Extragalactic Database (NED), which is operated by the Jet Propulsion Laboratory, California Institute of Technology, under contract with the National Aeronautics and Space Administration. This research has made use of the SIMBAD database, operated at CDS, Strasbourg, France.

The Pan-STARRS1 Surveys (PS1) and the PS1 public science archive have been made possible through contributions by the Institute for Astronomy, the University of Hawaii, the Pan-STARRS Project Office, the Max-Planck Society and its participating institutes, the Max Planck Institute for Astronomy, Heidelberg and the Max Planck Institute for Extraterrestrial Physics, Garching, The Johns Hopkins University, Durham University, the University of Edinburgh, the Queen’s University Belfast, the Harvard-Smithsonian Center for Astrophysics, the Las Cumbres Observatory Global Telescope Network Incorporated, the National Central University of Taiwan, the Space Telescope Science Institute, the National Aeronautics and Space Administration under Grant No. NNX08AR22G issued through the Planetary Science Division of the NASA Science Mission Directorate, the National Science Foundation grant no. AST-1238877, the University of Maryland, Eotvos Lorand University (ELTE), the Los Alamos National Laboratory, and the Gordon and Betty Moore Foundation.

This publication makes use of data products from the 2MASS, which is a joint project of the University of Massachusetts and the Infrared Processing and Analysis Center/California Institute of Technology, funded by the National Aeronautics and Space Administration and the National Science Foundation.

This publication makes use of data products from the *WISE*, which is a joint project of the University of California, Los Angeles, and the Jet Propulsion Laboratory/California Institute of Technology, funded by the National Aeronautics and Space Administration.

The authors are grateful to Dr S. Ciroi for helpful discussion on the topic of FFA.

TS was partly supported by the Academy of Finland project 315721.

TH was supported by the Academy of Finland projects 317383, 320085, 322535, and 345899.

SK acknowledges support from the European Research Council (ERC) under the European Union’s Horizon 2020 research and innovation programme under grant agreement no. 771282.

IV would like to thank the Magnus Ehrnrooth Foundation for their continuing support.

RR and WM are supported by the ANID BASAL project FB210003.

DATA AVAILABILITY

The JVLA (Legacy ID: AJ442) and the VLBA (Legacy ID: BJ109) data are publicly available in the NRAO Data Archive: <https://data.nrao.edu>. The MRO and OVRO data will be made available via CDS.

REFERENCES

Abdo A. A. et al., 2009, *ApJ*, 699, 976

Acciari V. A. et al., 2014, *Astropart. Phys.*, 54, 1

Alexander K. D., van Velzen S., Horesh A., Zauderer B. A., 2020, *Space Sci. Rev.*, 216, 81

Araudo A. T., Bosch-Ramon V., Romero G. E., 2010, *A&A*, 522, A97

Araudo A. T., Bosch-Ramon V., Romero G. E., 2013, *MNRAS*, 436, 3626

Baars J. W. M., Genzel R., Pauliny-Toth I. I. K., Witzel A., 1977, *A&A*, 61, 99

Bakala P., Bakalová A., La Placa R., Falanga M., Stella L., 2023, *A&A*, 673, A164

Bannister K. W., Stevens J., Tuntsov A. V., Walker M. A., Johnston S., Reynolds C., Bignall H., 2016a, *Science*, 351, 354

Bannister K., Bignall H., Johnston S., Reynolds C., Stevens J., Tuntsov A., Walker M., 2016b, *Astron. Telegram*, 8696, 1

Bardeen J. M., Petterson J. A., 1975, *ApJ*, 195, L65

Becker R. H., White R. L., Helfand D. J., 1995, *ApJ*, 450, 559

Begelman M. C., Blandford R. D., Rees M. J., 1980, *Nature*, 287, 307

Belladitta S. et al., 2022, *A&A*, 660, A74

Berton M. et al., 2017, *Front. Astron. Space Sci.*, 4, 8

Berton M. et al., 2018, *A&A*, 614, A87

Berton M. et al., 2020b, *A&A*, 636, A64

Berton M., Björklund I., Lähteenmäki A., Congiu E., Järvelä E., Terreran G., La Mura G., 2020a, *Contrib. Astron. Obs. Skalnate Pleso*, 50, 270

Boroson T. A., Green R. F., 1992, *ApJS*, 80, 109

Bosch-Ramon V., Perucho M., Barkov M. V., 2012, *A&A*, 539, A69

Caccianiga A. et al., 2015, *MNRAS*, 451, 1795

Campana S., Mainetti D., Colpi M., Lodato G., D'Avanzo P., Evans P. A., Moretti A., 2015, *A&A*, 581, A17

Chambers K. C. et al., 2016, preprint ([arXiv:1612.05560](https://arxiv.org/abs/1612.05560))

Chen S. et al., 2020, *MNRAS*, 498, 1278

Chen S. et al., 2022, *MNRAS*, 512, 471

Cinò G., Beckert T., Krichbaum T. P., Fuhrmann L., Kraus A., Witzel A., Zensus J. A., 2002, *Publ. Astron. Soc. Aust.*, 19, 10

Clausen-Brown E., Lyutikov M., Kharb P., 2011, *MNRAS*, 415, 2081

Condon J. J., 1992, *ARA&A*, 30, 575

Condon J. J., Cotton W. D., Greisen E. W., Yin Q. F., Perley R. A., Taylor G. B., Broderick J. J., 1998, *AJ*, 115, 1693

Condon J. J., Ransom S. M., 2016, *Essential Radio Astronomy*. Princeton University Press, Princeton, NJ

Congiu E. et al., 2023, *A&A*, 672, A148

Costamante L., Cutini S., Tosti G., Antolini E., Tramacere A., 2018, *MNRAS*, 477, 4749

Czerny B., Siemiginowska A., Janiuk A., Nikiel-Wroczyński B., Stawarz Ł., 2009, *ApJ*, 698, 840

de Gouveia Dal Pino E. M., Piovezan P. P., Kadowaki L. H. S., 2010, *A&A*, 518, A5

del Palacio S., Bosch-Ramon V., Romero G. E., 2019, *A&A*, 623, A101

Doi A., Asada K., Nagai H., 2011, *ApJ*, 738, 126

Doi A., Oyama T., Kono Y., Yamauchi A., Suzuki S., Matsumoto N., Tazaki F., 2016, *PASJ*, 68, 73

Du P. et al., 2018, *ApJ*, 856, 6

Duchesne S. W. et al., 2024, *Publ. Astron. Soc. Aust.*, 41, 3

Fedorova E., Del Popolo A., 2023, *Universe*, 9, 212

Ferland G. J., Peterson B. M., Horne K., Welsh W. F., Nahar S. N., 1992, *ApJ*, 387, 95

Fiedler R. L., Dennison B., Johnston K. J., Hewish A., 1987, *Nature*, 326, 675

Foschini L. et al., 2015, *A&A*, 575, A13

Foschini L. et al., 2021, *Universe*, 7, 372

Foschini L. et al., 2022, *Universe*, 8, 587

Fraix-Burnet D., 1992, *A&A*, 259, 445

Frederick S. et al., 2021, *ApJ*, 920, 56

Gabuzda D., 2018, *Galaxies*, 7, 5

Gaskell C. M., 2009, *New Astron. Rev.*, 53, 140

Ghisellini G., Tavecchio F., 2008, *MNRAS*, 386, L28

Giannios D., 2013, *MNRAS*, 431, 355

Giannios D., Uzdensky D. A., Begelman M. C., 2009, *MNRAS*, 395, L29

Gómez J.-L., Marscher A. P., Alberdi A., Jorstad S. G., García-Miró C., 2000, *Science*, 289, 2317

Goodrich R. W., 1989, *ApJ*, 342, 224

Gordon Y. A. et al., 2021, *ApJS*, 255, 30

Greene J. E., Ho L. C., 2005, *ApJ*, 630, 122

Greisen E. W., 2003, Heck A.ed., ASSL Vol. 285, *Information Handling in Astronomy - Historical Vistas*. Kluwer Academic Publishers, Dordrecht, p. 109

Heckman T. M., Best P. N., 2014, *ARA&A*, 52, 589

Helfand D. J., White R. L., Becker R. H., 2015, *ApJ*, 801, 26

Homan D. C. et al., 2021, *ApJ*, 923, 67

Homan D. C., Lister M. L., 2006, *AJ*, 131, 1262

Horton M. A., Hardcastle M. J., Read S. C., Krause M. G. H., 2020, *MNRAS*, 493, 3911

Hovatta T., Valtaoja E., Tornikoski M., Lähteenmäki A., 2009, *A&A*, 494, 527

Intema H. T., Jagannathan P., Mooley K. P., Frail D. A., 2017, *A&A*, 598, A78

Järvelä E., Berton M., Crepaldi L., 2021, *Front. Astron. Space Sci.*, 8, 147

Järvelä E., Dahale R., Crepaldi L., Berton M., Congiu E., Antonucci R., 2022, *A&A*, 658, A12

Järvelä E., Lähteenmäki A., Berton M., 2018, *A&A*, 619, A69

Järvelä E., Lähteenmäki A., León-Tavares J., 2015, *A&A*, 573, A76

Järvelä E., Lähteenmäki A., Lietzen H., Poudel A., Heinämäki P., Einasto M., 2017, *A&A*, 606, A9

Kadowaki L. H. S., de Gouveia Dal Pino E. M., Singh C. B., 2015, *ApJ*, 802, 113

Kara E. et al., 2012, *ApJ*, 746, 159

Kardashev N. S., 1962, *Astron. Zh.*, 39, 393

Kellermann K. I., Sramek R., Schmidt M., Shaffer D. B., Green R., 1989, *AJ*, 98, 1195

Kimura S. S., Toma K., Noda H., Hada K., 2022, *ApJ*, 937, L34

King A. R., Pringle J. E., West R. G., Livio M., 2004, *MNRAS*, 348, 111

Kino M. et al., 2021, *ApJ*, 920, L24

Klein U., Lisenfeld U., Verley S., 2018, *A&A*, 611, A55

Kollatschny W., Zetel M., 2011, *Nature*, 470, 366

Komissarov S. S., Gubanov A. G., 1994, *A&A*, 285, 27

Komossa S., Voges W., Xu D., Mathur S., Adorf H.-M., Lemson G., Duschl W. J., Grupe D., 2006, *AJ*, 132, 531

Komossa S., Xu D. W., Wagner A. Y., 2018, *MNRAS*, 477, 5115

Kovalev Y. Y., Pushkarev A. B., Nokhrina E. E., Plavin A. V., Beskin V. S., Chernoglazov A. V., Lister M. L., Savolainen T., 2020, *MNRAS*, 495, 3576

Król D. Ł., Stawarz Ł., Krzesinski J., Cheung C. C., 2023, *ApJ*, 943, 171

Kudryavtseva N. A. et al., 2011, *A&A*, 526, A51

Lacy M. et al., 2020, *PASP*, 132, 035001

Lähteenmäki A. et al., 2017, *A&A*, 603, A100

Lähteenmäki A., Järvelä E., Ramakrishnan V., Tornikoski M., Tammi J., Vera R. J. C., Chamani W., 2018, *A&A*, 614, L1

Lähteenmäki A., Valtaoja E., Wiik K., 1999, *ApJ*, 511, 112

Lalakos A. et al., 2022, *ApJ*, 936, L5

Laor A., 2000, *ApJ*, 543, L111

Liao N. H., Bai J. M., 2015, *New Astron.*, 34, 134

Liska M. T. P., Musoke G., Tchekhovskoy A., Porth O., Beloborodov A. M., 2022, *ApJ*, 935, L1

Liska M., Hesp C., Tchekhovskoy A., Ingram A., van der Klis M., Markoff S., 2018, *MNRAS*, 474, L81

Lister M. L. et al., 2016, *AJ*, 152, 12

Livio M., Pringle J. E., King A. R., 2003, *ApJ*, 593, 184

Lohfink A. M. et al., 2013, *ApJ*, 772, 83

Macquart J. P., Shannon R. M., Bannister K. W., James C. W., Ekers R. D., Bunton J. D., 2019, *ApJ*, 872, L19

Mathur S., 2000, *MNRAS*, 314, L17

McKinney J. C., Chluba J., Wielgus M., Narayan R., Sadowski A., 2017, *MNRAS*, 467, 2241

Mhaskey M., Paul S., Krishna G., 2021, *Astron. Nachr.*, 342, 1126

Mignone A., Rossi P., Bodo G., Ferrari A., Massaglia S., 2010, *MNRAS*, 402, 7

Miville-Deschénes M.-A., Lagache G., 2005, *ApJS*, 157, 302

Nalewajko K., Giannios D., Begelman M. C., Uzdensky D. A., Sikora M., 2011, *MNRAS*, 413, 333

Neugebauer G. et al., 1984, *ApJ*, 278, L1

Nyland K. et al., 2020, *ApJ*, 905, 74

O'Dea C. P., Saikia D. J., 2021, *A&AR*, 29, 3

Olguín-Iglesias A., Kotilainen J., Chavushyan V., 2020, *MNRAS*, 492, 1450

Osterbrock D. E., Pogge R. W., 1985, *ApJ*, 297, 166

Padovani P., 2017, *Nat. Astron.*, 1, 0194

Paliya V. S., 2019, *J. Astrophys. Astron.*, 40, 39

Peirson A. L. et al., 2022, *ApJ*, 927, 24

Peterson B. M., 2011, preprint (arXiv:1109.4181)

Petroff E., Hessels J. W. T., Lorimer D. R., 2022, *A&AR*, 30, 2

Poutanen J., Stern B., 2010, *ApJ*, 717, L118

Pringle J. E., 1996, *MNRAS*, 281, 357

Pushkarev A. B. et al., 2013, *A&A*, 555, A80

Raiteri C. M. et al., 2017, *Nature*, 552, 374

Raiteri C. M. et al., 2021, *MNRAS*, 501, 1100

Rani B. et al., 2013, *A&A*, 552, A11

Readhead A. C. S., 1994, *ApJ*, 426, 51

Richards J. L. et al., 2011, *ApJS*, 194, 29

Richards J. L. et al., 2015, Massaro F., Cheung C. C., Lopez E., Siemiginowska A. eds, IAU Symp. Vol. 313, Extragalactic Jets from Every Angle. Cambridge University Press, Cambridge, p.139,

Richards J. L., Hovatta T., Max-Moerbeck W., Pavlidou V., Pearson T. J., Readhead A. C. S., 2014, *MNRAS*, 438, 3058

Richards J. L., Lister M. L., 2015, *ApJ*, 800, L8

Ripperda B., Liska M., Chatterjee K., Musoke G., Philippov A. A., Markoff S. B., Tchekhovskoy A., Younsi Z., 2022, *ApJ*, 924, L32

Rodriguez L. F., Martí J., Canto J., Moran J. M., Curiel S., 1993, *Rev. Mex. Astron. Astrofis.*, 25, 23

Romano P. et al., 2023, *A&A*, 673, A85

Romano P., Vercellone S., Foschini L., Tavecchio F., Landoni M., Knöldlseder J., 2018, *MNRAS*, 481, 5046

Romero G. E., Cellone S. A., Combi J. A., 2000, *A&A*, 360, L47

Romero G. E., Cellone S. A., Combi J. A., Andruhov I., 2002, *A&A*, 390, 431

Ross K., Hurley-Walker N., Seymour N., Callingham J. R., Galvin T. J., Johnston-Hollitt M., 2022, *MNRAS*, 512, 5358

Sani E., Lutz D., Risaliti G., Netzer H., Gallo L. C., Trakhtenbrot B., Sturm E., Boller T., 2010, *MNRAS*, 403, 1246

Savolainen T. et al., 2023, *A&A*, 676, A114

Shepherd M. C., 1997, Hunt G., Payne H. eds, ASP Conf. Ser. Vol. 125, Astronomical Data Analysis Software and Systems VI, Astronomical Society of the Pacific, San Francisco, p.77

Shimwell T. W. et al., 2022, *A&A*, 659, A1

Shukla A., Mannheim K., 2020, *Nat. Commun.*, 11, 4176

Skrutskie M. F. et al., 2006, *AJ*, 131, 1163

Steffen W., 1997, *Vistas Astron.*, 41, 71

Sulentic J. W., Zwicker T., Marziani P., Dultzin-Hacyan D., 2000, *ApJ*, 536, L5

Teräranta H. et al., 1998, *A&AS*, 132, 305

Thirring H., 1918, *Phys. Z.*, 19, 33

Torniainen I., Tornikoski M., Teräranta H., Aller M. F., Aller H. D., 2005, *A&A*, 435, 839

Tornikoski M. et al., 2009, *Astron. Nachr.*, 330, 128

Tornikoski M., Jussila I., Johansson P., Lainela M., Valtaoja E., 2001, *AJ*, 121, 1306

Valtaoja E., Lähteenmäki A., Teräranta H., Lainela M., 1999, *ApJS*, 120, 95

Varglund I., Järvelä E., Lähteenmäki A., Berton M., Ciroi S., Congiu E., 2022, *A&A*, 668, A91

Vedantham H. K. et al., 2017, *ApJ*, 845, 89

Villata M., Raiteri C. M., 1999, *A&A*, 347, 30

Vovk I., Neronov A., 2013, *ApJ*, 767, 103

Wagner A. Y., Bicknell G. V., Umemura M., 2012, *ApJ*, 757, 136

Wang F. et al., 2016, *ApJ*, 824, 149

Winkel N. et al., 2022, *A&A*, 663, A104

Wright E. L. et al., 2010, *AJ*, 140, 1868

Yuan W., Zhou H. Y., Komossa S., Dong X. B., Wang T. G., Lu H. L., Bai J. M., 2008, *ApJ*, 685, 801

APPENDIX A: DETAILS OF OBSERVATIONS

Here, we provide some further details regarding the observations and the data reduction procedures.

A1 JVLA and VLBA

Table A1 summarizes the JVLA observations, including the date of the observation for each source, and the integration times in all bands. The VLBA observations, including the name of the calibrator source, its distance from the target as well as its VLBI scale flux density at 15 GHz, and the phase referencing cycle time of the observation are summarized in Table A2.

A2 MRO

The quality of the MRO data and the reliability of the detections are constantly monitored through several semi-automatic and manual checks. Measurements that are considered to be of poor quality, for example, due to unfavourable weather conditions or other environmental effects, are discarded semi-automatically. Additionally, faint detections are checked manually in the final data reduction stage.

Table A1. Summary of the JVLA observations.

Source	Date (yyyy-mm-dd)	$T_{\text{int}} (X/Ku/Ka/Q)$ (s)
J1029+5556	2022-04-22	594/594/534/706/754
J1228+5018	2022-04-24	596/596/532/706/754
J1232+4957	2022-04-25	594/594/532/708/754
J1509+6137	2022-03-26	594/594/532/590/754
J1510+5547	2022-03-13	594/594/534/706/868
J1522+3934	2022-03-16	594/594/532/704/810
J1641+3454	2022-03-15	594/594/543/708/696

Notes. Columns: (1) source name; (2) date of observations; and (3) integration time in each band.

Table A2. Summary of the VLBA observations.

Source	Calibrator	Distance (deg)	$S_{v,\text{cal}}$ (mJy)	T_{cycle} (s)
J1029+5556	J1035+5628	0.99	300	180
J1228+5018	J1223+5037	0.87	62	160
J1232+4957	J1223+5037	1.53	62	160
J1509+6137	J1526+6110	2.05	38	220
J1510+5547	J1510+5702	1.26	200	160
J1522+3934	J1528+3816	1.82	68	200
J1641+3454	J1635+3458	1.21	190	180

Notes. Columns: (1) target source name; (2) phase reference calibrator; (3) distance between the target and the calibrator; (4) calibrator's VLBI scale flux density at 15 GHz; and (5) phase referencing cycle time.

The general flux density levels are checked to be consistent with adjacent measurements (i.e. other sources observed before and after the target source). In addition, we checked if the observations of these NLS1s could be contaminated by a bright radio source falling into the reference beam of the MRO telescope. Using LoTSS, FIRST, and VLASS data, we concluded that whereas there are a few moderately bright sources with flux densities around a few hundred mJy at low radio frequencies that could be in the reference beam, all of them have steep spectra, and it is thus very unlikely that any of them could affect these observations.

Due to the fairly high detection limit of the telescope (i.e. approx. 200 mJy in optimal conditions, which is more than adequate for the bright AGN monitoring programmes conducted at MRO), we typically only see the highest tips of the flares in faint sources, whereas most of the lower level activity remains below the detection threshold (e.g. Acciari et al. 2014). This is also seen in the upper limits, the level of which can drastically change in even a short time due to compromised weather conditions that can also significantly raise the detection limit. The undetected source could be actually fainter due to variability or the observing conditions could be worse (or both), and it is therefore not detected. The upper limits describe the largest flux density the source could have in the current conditions but still remain below the 4σ detection limit and cannot therefore be used for data analysis. However, it has been shown that the high activity periods of NLS1 sources detected at MRO correspond to flare peaks in OVRO data (Lähteenmäki et al. 2017), confirming that at least most of the time the two telescopes are catching the same events.

A2.1 Additional checks

In addition to all the aforementioned measures to eliminate compromised observations, a series of additional checks were conducted to identify possible sources causing anomalous detections. The following issues were addressed: saturation of the Peltier cooling element, the effect of the pointing model, drift, contamination by astronomical or terrestrial radio sources such as conspicuous but rare flux density increases caused by aircraft in the telescope beam, and pure statistical chance. All these checks will be discussed in detail below.

Saturation of the Peltier cooling element. During hot summer days or due to prolonged heating of the radome, for example, to melt snow, the Peltier element can saturate, leading to insufficient cooling of the receiver, and a rapidly changing local oscillator (LO) power. Using several observations during which the Peltier element saturated but the observing conditions were otherwise good, we investigated what is the impact of the rapid and drastic changes in the LO power. We concluded that there is no considerable drift in the signal during any of these observations, the levels are as expected, and the errors match values considered very good during summer conditions – thus, no clear, dramatic effects on the data are seen. Even though the LO power level changes seem rather fast, the long integration times of our observations essentially help in mitigating this problem.

Inaccurate pointing model. The pointing of the MRO telescope is determined with 5-point (5p) observations of bright (>5 Jy) sources. Due to the lack of consistently bright sources in the Northern sector, the pointing model in that region of the sky is known to be insufficient, possibly leading to equivocal variability. A thorough investigation of the Northern anomaly is currently ongoing, however, there are several reasons why this is an unlikely explanation for the variability we see in our sources. First, inaccurate pointing leads to decreased

flux densities, not increased; second, the NLS1 data do not show confirmed direction-dependent trends; and third, the detectability or maximum brightness (and thus maximum variability) of our sources do not depend on the declination.

Drift. The MRO observing system monitors and reports the changes in the intensity levels within the integration. The difference between the maximum and minimum result of the primary beam of the telescope is constantly calculated during the observation and reported as *drift*. It is typically caused by weather and environmental conditions, and can either increase or decrease the final flux density value, depending on which beam it starts on. The observing system alerts the observer when notable drift is seen. The drift limits are rather conservative, meaning that alerts are often given also when the data quality throughout the integration is considered acceptable. The avoidance system with the alerts and the human intervention by both the observer and the data reducer are considered enough to guarantee that no false positives induced solely by the drift are likely.

Contamination by astronomical radio sources. The possibility of other extragalactic radio sources falling into the MRO beam was already discussed earlier and is deemed very unlikely. Additionally, the MRO observing system gives a warning when a source is too close to the Sun or the Moon. No such checks are made for the planets. However, the chances of having them within the beam is naturally rather small, and, especially for consecutive detections for the same source typically taken days or weeks apart, the distance to the planet would have changed.

Contamination by terrestrial radio sources. At radio frequencies, interference from a plethora of terrestrial sources is known to affect astronomical observations. At MRO, the radio frequency interference (RFI) environment at frequency bands lower than the signal frequency is closely monitored and tests with different sources of radio emission have been conducted. The sources of RFI vary from mobile phones to faulty LED light bulbs. These can show up as added noise levels or interference at MRO's intermediate frequencies, but there are no documented cases where they would have shown up as clear spikes in the 37 GHz data. What has been shown to cause a high-intensity spike at 37 GHz is an aeroplane as a black body passing through the beam. This effect is seen as a fast, typically 0.3 s spike. Even though fast, the spike is very strong, typically several tens of times higher in amplitude than the actual source; for example, one of the first such spikes discovered was ~ 160 Jy. Because it is very fast, the impact on the final data is not dramatic and usually shows up as a larger-than-expected error. MRO has a warning system for detecting such spikes and the observers are also instructed to look for such spikes in the data. During data reduction anomalous cases of high errors or odd flux densities always lead to a proper investigation of the auxiliary data and plots, which reveals these spikes.

Statistical chance. According to the central limit theorem (CLT), the sampling distribution of the mean will always be normally distributed as long as the sample size is large enough, independent of the original distribution. We can thus use the one-tail normal distribution to estimate the number of false detections arising from this condition. The CLT dictates that a false 4σ detection should occur once in every 31 546 data points. This is rare but not impossible, whereas successive false detections are extremely rare. However, in reality changing conditions make estimating the noise sigma difficult and a perfect normal distribution is not guaranteed. If the number of false detections at different sigma levels significantly deviates from the predicted numbers it could mean that there are unknown factors in play, possibly increasing the chances of obtaining anomalous detections. This is currently being tested at MRO by introducing a fake test source at a sky position as clear of radio sources as

possible. Three test runs have been completed so far, resulting in ~ 60 observations of empty radio sky. Out of these observations, none exceeded 3σ , two were 2σ – 3σ , and the rest $< 2\sigma$. The CLT predicts 2.3 2σ and 0.135 3σ measurements per one hundred repetitions, and thus the results of observing the empty sky region seem to be in line with theory. However, more observations need to and will be performed to improve the statistics. Either way, these observations resulted in zero detections, indicating that there do not seem to be systematic sources of error leading to false detections at the rates we see in our sources.

Based on all the checks described in this section, we were unable to identify viable sources of false detections. In principle, some unknown effect causing this phenomenon can exist, but it should also affect all the other AGN monitored at MRO, and no signs of this kind of behaviour have been seen when investigating the detectability of other faint AGN samples. To the best of our knowledge, these NLS1 detections are real and reliable.

A3 OVRO

The AGN monitoring sample at OVRO mostly consists of bright blazar-type objects, with the majority having a mean flux density > 60 mJy (Richards et al. 2014). Therefore in the schedules, each observation consists of four on–on integrations, each 8 s long, resulting in a total integration time of 32 s. Given the small number of on–on integrations, it is possible that atmospheric fluctuations or pointing errors result in outliers in the light curves (Richards et al. 2014). Moreover, the number of observations performed each day is large (up to 500) so that it is possible that some, apparently high S/N observations, occur purely due to random fluctuations. The data are processed with an automated pipeline, where manual editing is done to flag obviously bad periods of data, and data are automatically flagged based on large changes within the four on–on integrations and other diagnostics (see Richards et al. 2011, for details). However, individual data points are not typically manually inspected, as for the variability analysis of bright blazars, the effect of outliers in the data is small (Richards et al. 2014).

Because of the faintness of the NLS1 targets, we have done additional manual checks to inspect the quality of the detections, which we describe here. We note that in all the cases described below, the flux density of the spurious detection has been less than 20 mJy and mostly < 10 mJy, or the uncertainty has been larger than usual so that similar observations in our blazar light curves would not be as problematic.

The receiver records both right- and left-hand circular polarization separately with the final observation being a weighted average of the two. We can thus inspect the two values separately to verify that the source has been detected in both polarizations (here we assume that the circular polarization of the objects is negligible, as is the case for most blazars at 15 GHz (e.g. Homan & Lister 2006). This made us reject two spurious detections in J1232+4957. Additionally, we have inspected observations of other nearby sources to see whether there are data that have been automatically flagged in the pipeline

close to the observation of the NLS1, indicative of potentially poor observing conditions. This resulted in the rejection of one spurious detection in J1641+3454.

In 2021 October, we also changed the observing strategy of these NLS1 targets so that they are observed twice in a row in the schedules. This way we can see whether short-term atmospheric effects or bad conditions have resulted in spurious detections if the two consecutive observations show a large difference, as we would not expect large changes on a time-scale of ~ 1 min. This resulted in the rejection of single spurious detections in J1029+5556, J1509+6137, J1510+5547, and J1522+3934, all of which had moderate S/N values of ~ 4 –9.

The remaining detections in the paper either show detections in two consecutive observations (J1522+3934) or consistent flux densities in the right- and left-hand circular polarization and no apparent problems with nearby targets (J1029+5556, J1522+3934, and J1641+3454). However, we cannot fully exclude additional, unknown effects in the observations before 2021 October when the sources were observed only once in a row, especially in J1029+5556 and J1641+3454 that do not show any other detections in the OVRO light curves. J1522+3934 on the other hand seems more reliable because of its multiple detections.

APPENDIX B: RADIO MAPS

The JVLA radio maps with likely detections are shown here. This includes X -, Ku -, K -, Ka -, and Q -band maps of J1228+5017 (Figs B1–B5), X - and Ku -band maps of J1232+4957 (Figs B6–B7), X -, Ku -, K -, and Ka -band maps of J1522+3934 (Figs B8–B11), and X -, Ku -, K -, Ka -, and Q -band maps of J1641+3454 (Figs B12–B16).

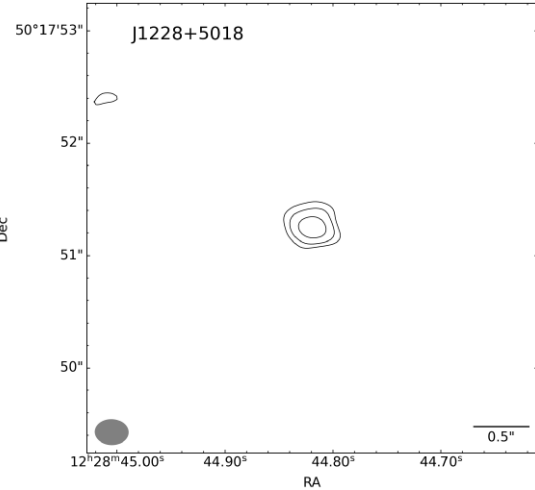


Figure B1. JVLA X-band radio map of J1228+5017, $\text{rms} = 7\mu\text{Jy beam}^{-1}$, contour levels at $-3, 3, 6, 12$ rms, and beam size 1.20 kpc \times 0.91 kpc (0.294 arcsec \times 0.223 arcsec).

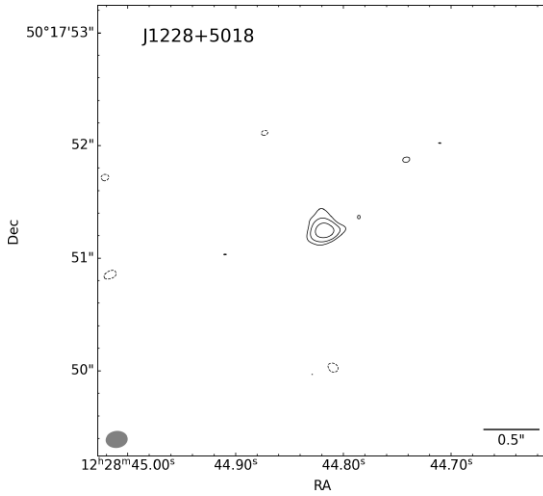


Figure B2. JVLA Ku-band radio map of J1228+5017, $\text{rms} = 6\mu\text{Jy beam}^{-1}$, contour levels at $-3, 3, 6, 12$ rms, and beam size $0.78 \text{ kpc} \times 0.58 \text{ kpc}$ ($0.191 \text{ arcsec} \times 0.142 \text{ arcsec}$).

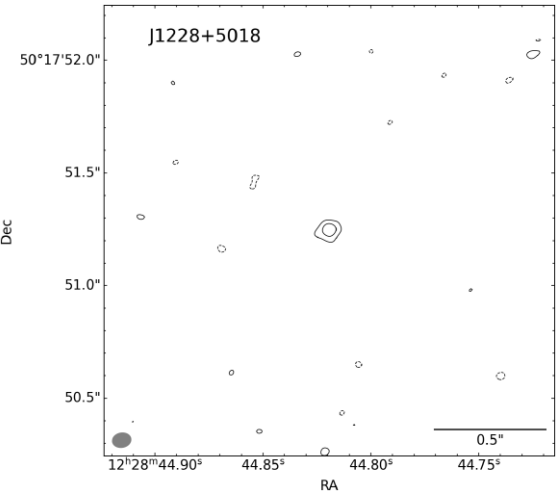


Figure B4. JVLA Ka-band radio map of J1228+5017, $\text{rms} = 12\mu\text{Jy beam}^{-1}$, contour levels at $-3, 3, 6$ rms, and beam size $0.34 \text{ kpc} \times 0.26 \text{ kpc}$ ($0.083 \text{ arcsec} \times 0.064 \text{ arcsec}$).

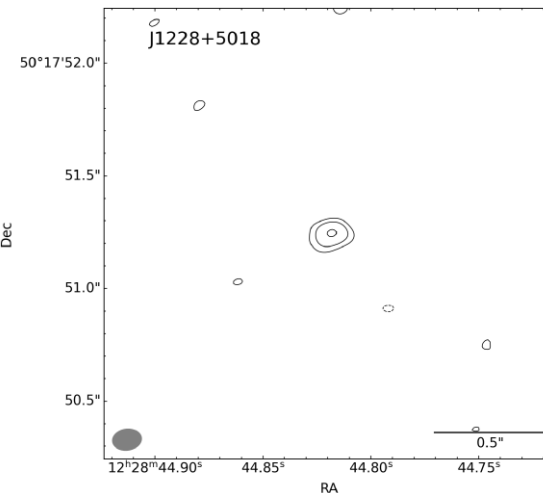


Figure B3. JVLA K-band radio map of J1228+5017, $\text{rms} = 9\mu\text{Jy beam}^{-1}$, contour levels at $-3, 3, 6, 12$ rms, and beam size $0.52 \text{ kpc} \times 0.38 \text{ kpc}$ ($0.129 \text{ arcsec} \times 0.094 \text{ arcsec}$).

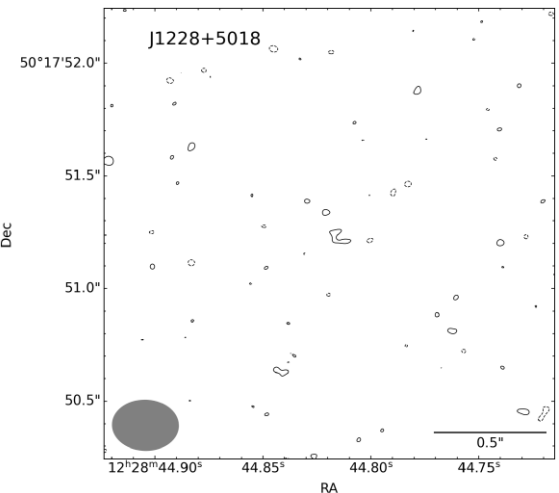


Figure B5. JVLA Q-band radio map of J1228+5017, $\text{rms} = 31\mu\text{Jy beam}^{-1}$, contour levels at $-3, 3$ rms, and beam size $0.24 \text{ kpc} \times 0.20 \text{ kpc}$ ($0.060 \text{ arcsec} \times 0.050 \text{ arcsec}$).

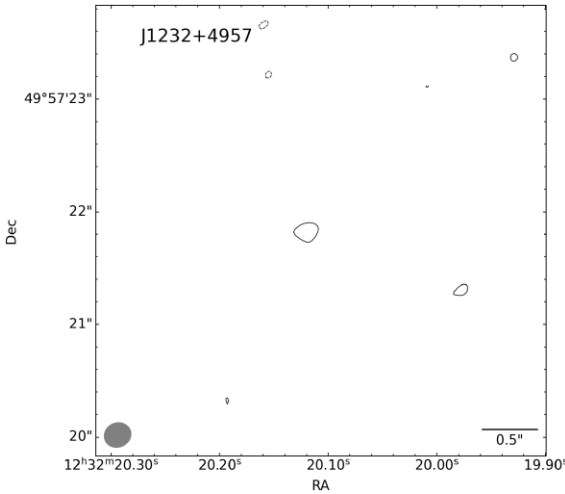


Figure B6. JVLA X-band radio map of J1232+4957, rms = $7\mu\text{Jy beam}^{-1}$, contour levels at $-3, 3$ rms, and beam size $0.98 \text{ kpc} \times 0.88 \text{ kpc}$ ($0.240 \text{ arcsec} \times 0.215 \text{ arcsec}$).

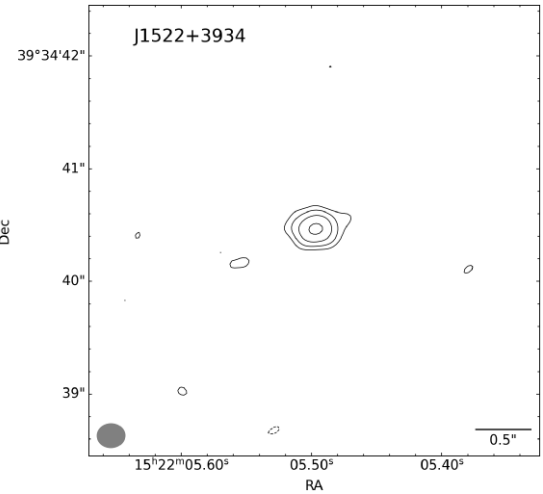


Figure B8. JVLA X-band radio map of J1522+3934, rms = $8\mu\text{Jy beam}^{-1}$, contour levels at $-3, 3, 6, 12, 24$ rms, and beam size $0.36 \text{ kpc} \times 0.31 \text{ kpc}$ ($0.248 \text{ arcsec} \times 0.213 \text{ arcsec}$).

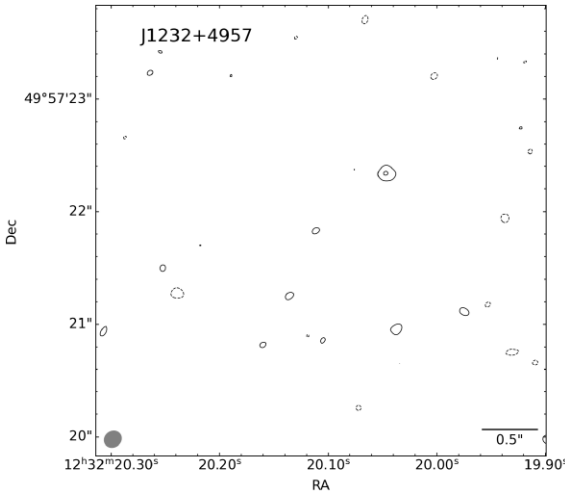


Figure B7. JVLA Ku-band radio map of J1232+4957, rms = $5\mu\text{Jy beam}^{-1}$, contour levels at $-3, 3, 6$ rms, and beam size $0.65 \text{ kpc} \times 0.57 \text{ kpc}$ ($0.159 \text{ arcsec} \times 0.141 \text{ arcsec}$).

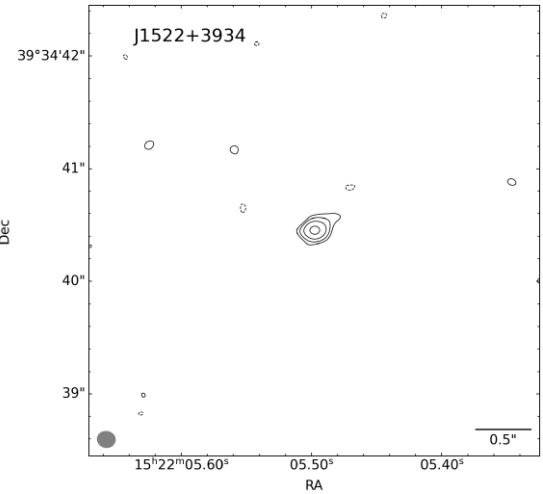


Figure B9. JVLA Ku-band radio map of J1522+3934, rms = $6\mu\text{Jy beam}^{-1}$, contour levels at $-3, 3, 6, 12, 24$ rms, and beam size $0.24 \text{ kpc} \times 0.21 \text{ kpc}$ ($0.162 \text{ arcsec} \times 0.142 \text{ arcsec}$).

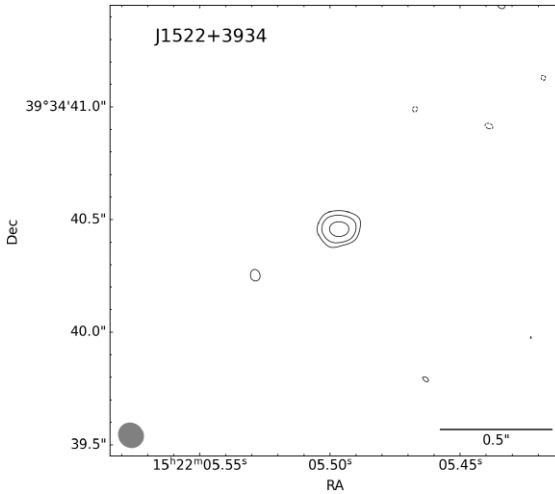


Figure B10. JVLA K -band radio map of J1522+3934, $\text{rms} = 9\mu\text{Jy beam}^{-1}$, contour levels at $-3, 3, 6, 12$ rms, and beam size $0.17 \text{ kpc} \times 0.16 \text{ kpc}$ ($0.114 \text{ arcsec} \times 0.106 \text{ arcsec}$).

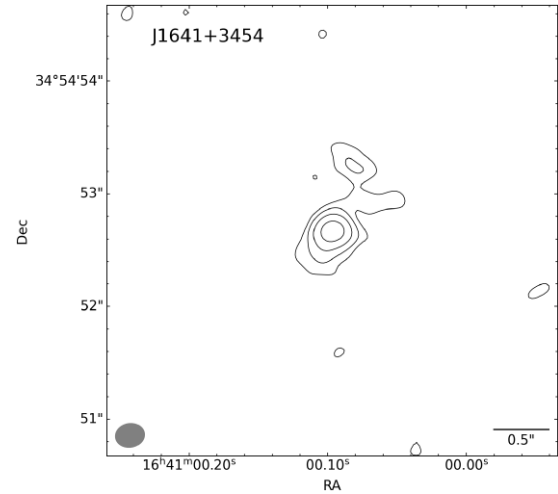


Figure B12. JVLA X -band radio map of J1641+3454, $\text{rms} = 7\mu\text{Jy beam}^{-1}$, contour levels at $-3, 3, 6, 12, 24$ rms, and beam size $0.73 \text{ kpc} \times 0.59 \text{ kpc}$ ($0.259 \text{ arcsec} \times 0.210 \text{ arcsec}$).

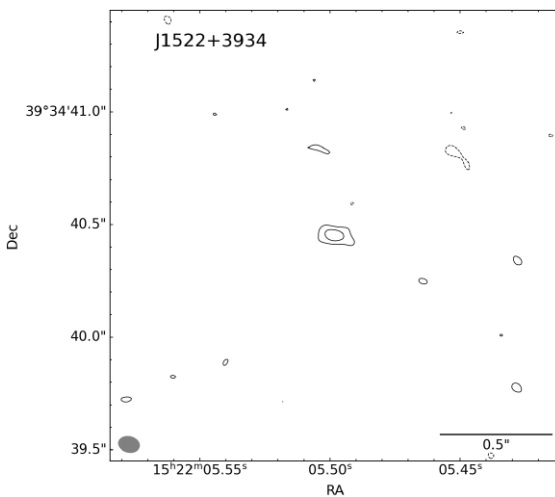


Figure B11. JVLA Ka -band radio map of J1522+3934, $\text{rms} = 13\mu\text{Jy beam}^{-1}$, contour levels at $-3, 3, 6$ rms, and beam size $0.10 \text{ kpc} \times 0.07 \text{ kpc}$ ($0.095 \text{ arcsec} \times 0.069 \text{ arcsec}$).

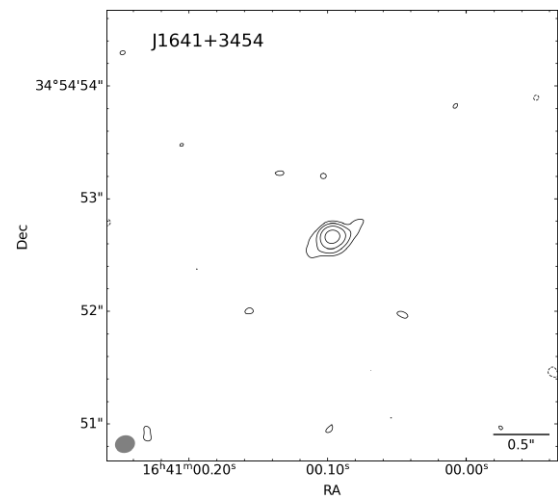


Figure B13. JVLA Ku -band radio map of J1641+3454, $\text{rms} = 5\mu\text{Jy beam}^{-1}$, contour levels at $-3, 3, 6, 12, 24$ rms, and beam size $0.49 \text{ kpc} \times 0.41 \text{ kpc}$ ($0.174 \text{ arcsec} \times 0.146 \text{ arcsec}$).

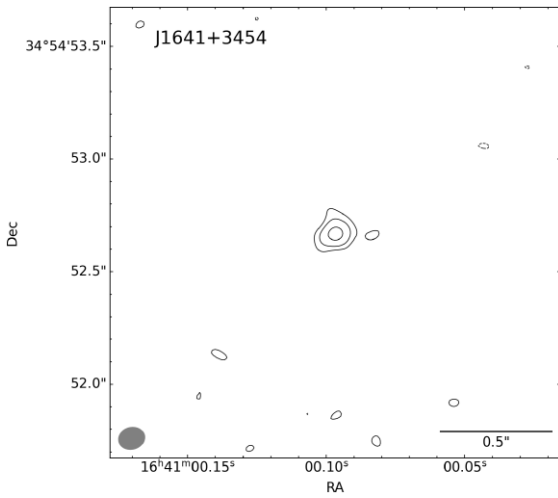


Figure B14. JVLA *K*-band radio map of J1641+3454, rms = $8\mu\text{Jy beam}^{-1}$, contour levels at $-3, 3, 6, 12$ rms, and beam size $0.33\text{ kpc} \times 0.27\text{ kpc}$ ($0.117\text{ arcsec} \times 0.096\text{ arcsec}$).

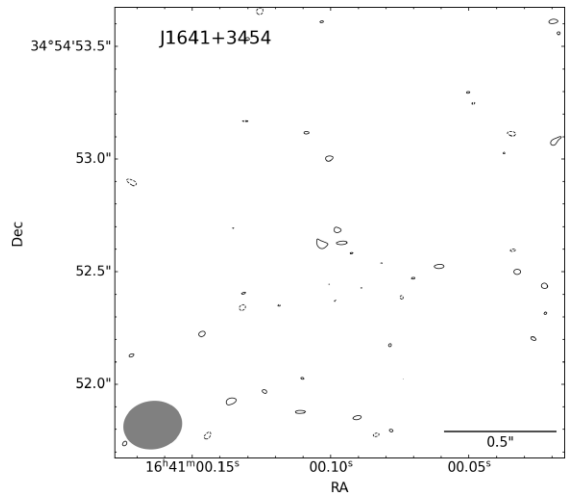


Figure B16. JVLA *Q*-band radio map of J1641+3454, rms = $33\mu\text{Jy beam}^{-1}$, contour levels at $-3, 3$ rms, and beam size $0.20\text{ kpc} \times 0.14\text{ kpc}$ ($0.071\text{ arcsec} \times 0.049\text{ arcsec}$).

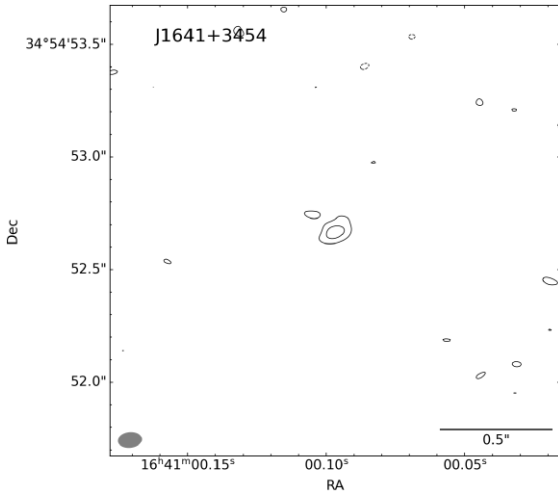


Figure B15. JVLA *Ka*-band radio map of J1641+3454, rms = $11\mu\text{Jy beam}^{-1}$, contour levels at $-3, 3, 6$ rms, and beam size $0.29\text{ kpc} \times 0.18\text{ kpc}$ ($0.103\text{ arcsec} \times 0.065\text{ arcsec}$).

APPENDIX C: LIGHT CURVES

The light curves of our sources from the beginning of 2014 to mid-2022 are shown here. Figs C1–C7 show light curves including low-resolution (MRO and OVRO) and high-resolution (JVLA, VLBA, and VLASS) data. Due to the strongly varying flux densities these plots are in logarithmic scale. The light curves in Figs C8–C14 show only the MRO and OVRO data in linear scale, and include also the 4σ upper limits for both observatories.

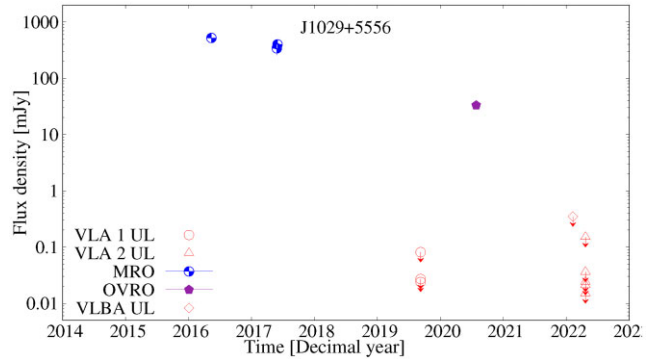


Figure C1. Light curve of J1029+5556. Symbols explained in the figure. Observed frequencies are: MRO 37 GHz, OVRO and VLBA 15 GHz, VLA 1 1.6, 5.2, and 9 GHz, and VLA 2 10, 15, 22, 33, and 45 GHz. Filled symbols denote integrated flux densities and empty symbols mark peak flux densities, except empty symbols with downward arrows that are used for upper limits. VLA 1 data from Berton et al. (2020b) and VLA 2 data from this paper.

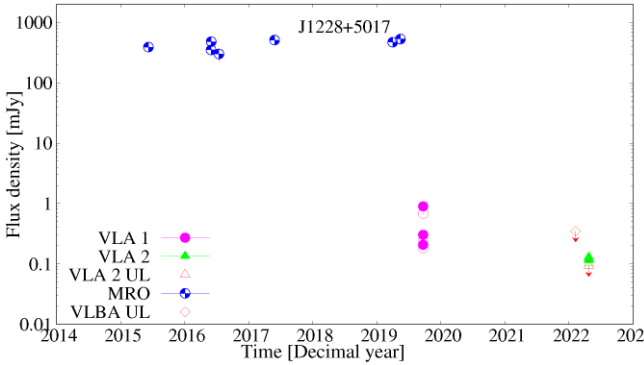


Figure C2. Light curve of J1228+5017. Symbols as in Fig. C1. Observed frequencies are: MRO 37 GHz, OVRO and VLBA 15 GHz, VLA 1 1.6, 5.2, and 9 GHz, and VLA 2 10, 15, 22, 33, and 45 GHz.

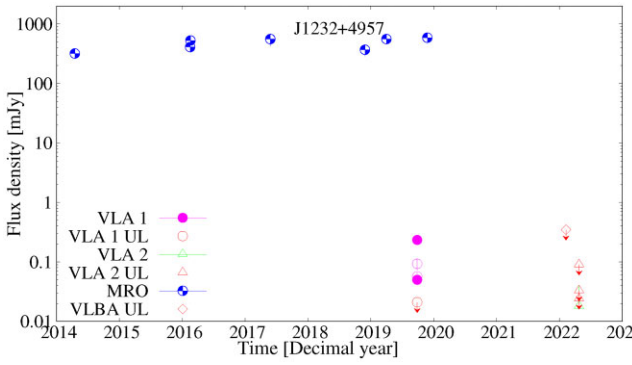


Figure C3. Light curve of J1232+4957. Symbols as in Fig. C1. Observed frequencies are: MRO 37 GHz, OVRO and VLBA 15 GHz, VLA 1 1.6, 5.2, and 9 GHz, VLA 2 10, 15, 22, 33, and 45 GHz.

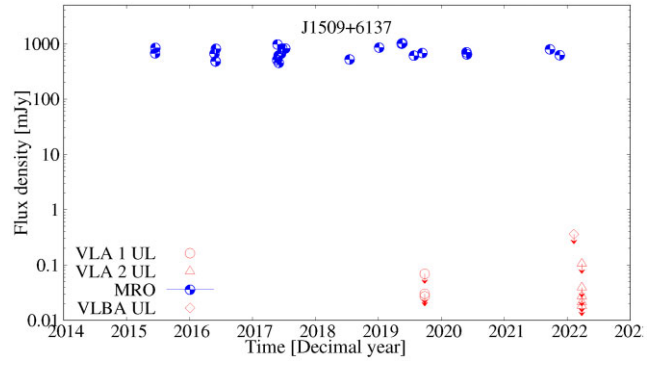


Figure C4. Light curve of J1509+6137. Symbols as in Fig. C1. Observed frequencies are: MRO 37 GHz, OVRO and VLBA 15 GHz, VLA 1 1.6, 5.2, and 9 GHz, and VLA 2 10, 15, 22, 33, and 45 GHz.

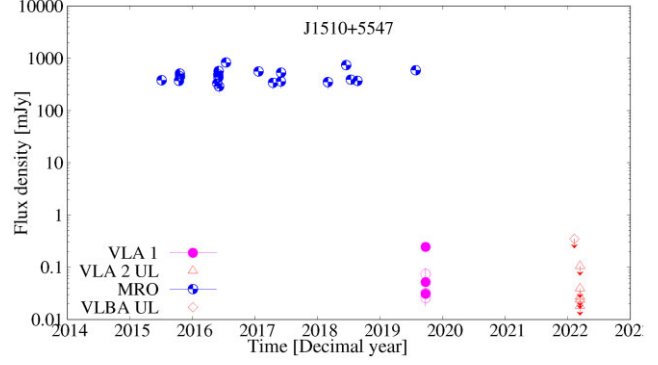


Figure C5. Light curve of J1510+5547. Symbols as in Fig. C1. Observed frequencies are: MRO 37 GHz, OVRO and VLBA 15 GHz, VLA 1 1.6, 5.2, and 9 GHz, and VLA 2 10, 15, 22, 33, and 45 GHz.

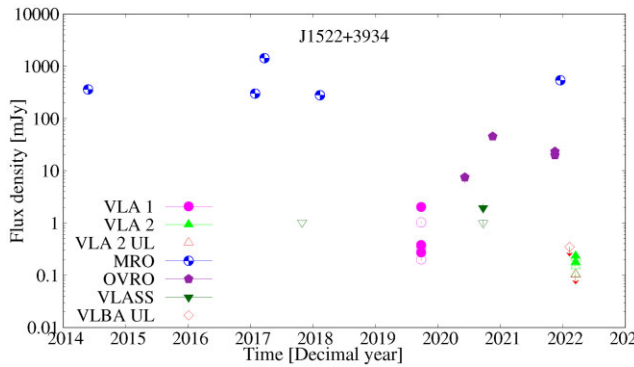


Figure C6. Light curve of J1522+3934. Symbols as in Fig. C1. Observed frequencies are: MRO 37 GHz, OVRO and VLBA 15 GHz, VLA 1 1.6, 5.2, and 9 GHz, VLA 2 10, 15, 22, 33, and 45 GHz, and VLASS 3 GHz.

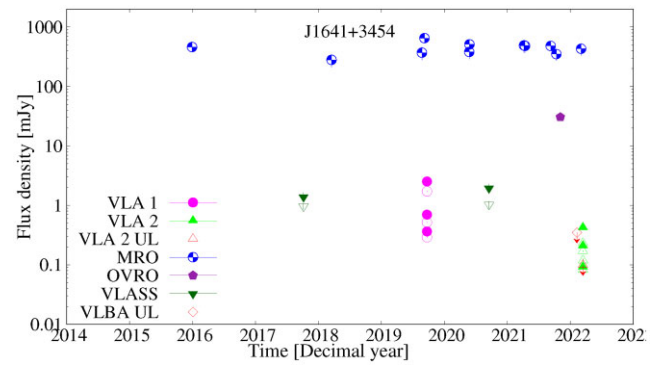


Figure C7. Light curve of J1641+3454. Symbols as in Fig. C1. Observed frequencies are: MRO 37 GHz, OVRO and VLBA 15 GHz, VLA 1 1.6, 5.2, and 9 GHz, VLA 2 10, 15, 22, 33, and 45 GHz, and VLASS 3 GHz.

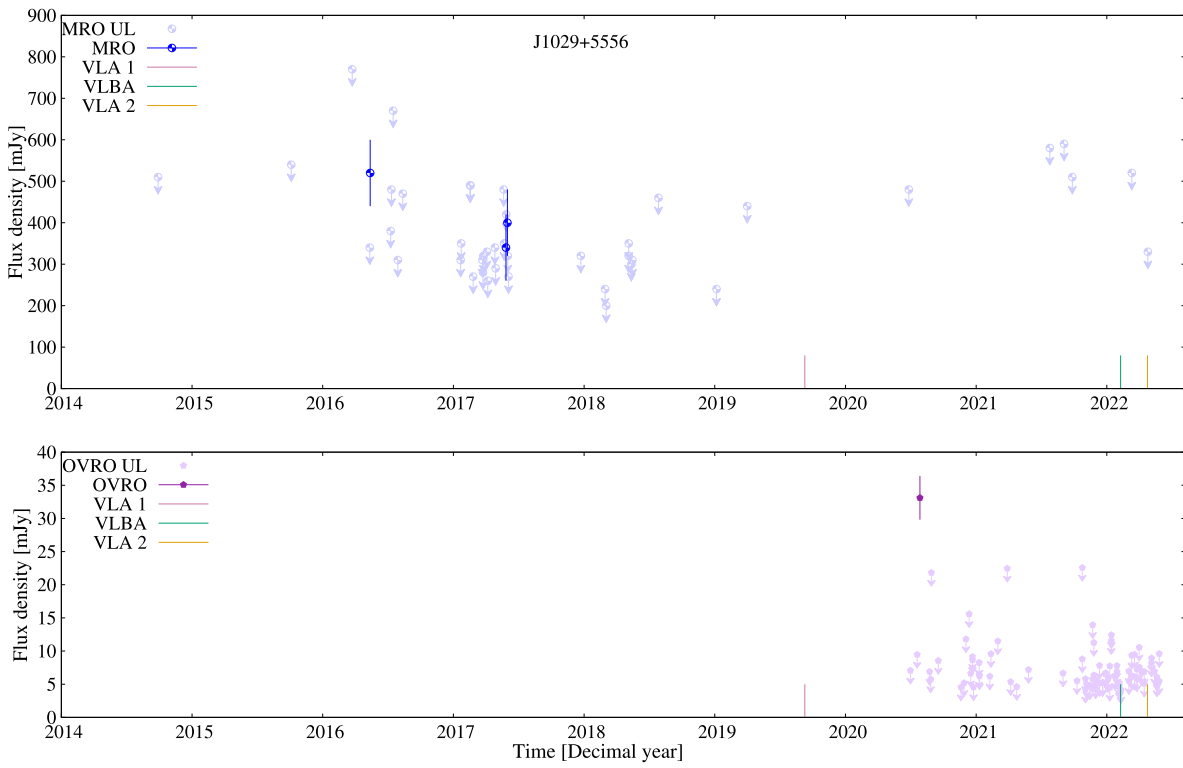


Figure C8. MRO (37 GHz) and OVRO (15 GHz) light curves of J1029+5556. Symbols are explained in the figure. Symbols with downward arrows denote upper limits, for the JVLA and the VLBA only the epochs of the observations are marked.

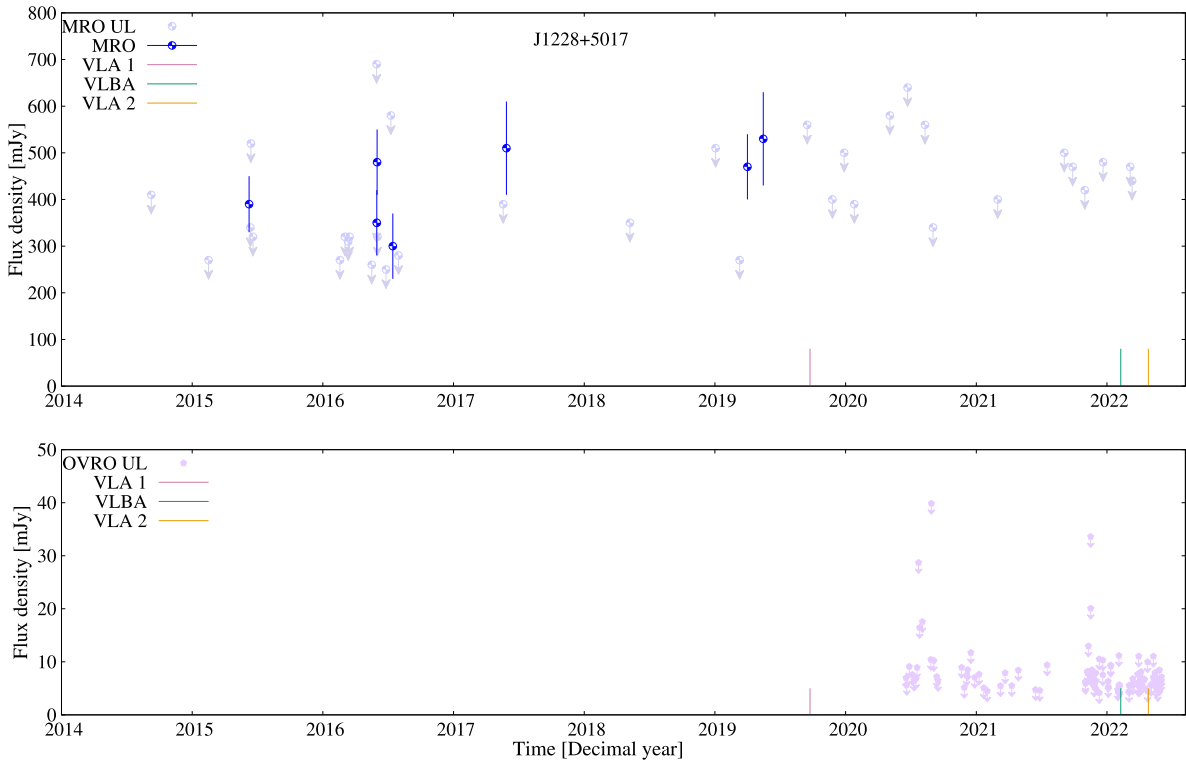


Figure C9. MRO (37 GHz) and OVRO (15 GHz) light curves of J1228+5017. Symbols as in Fig. C8.

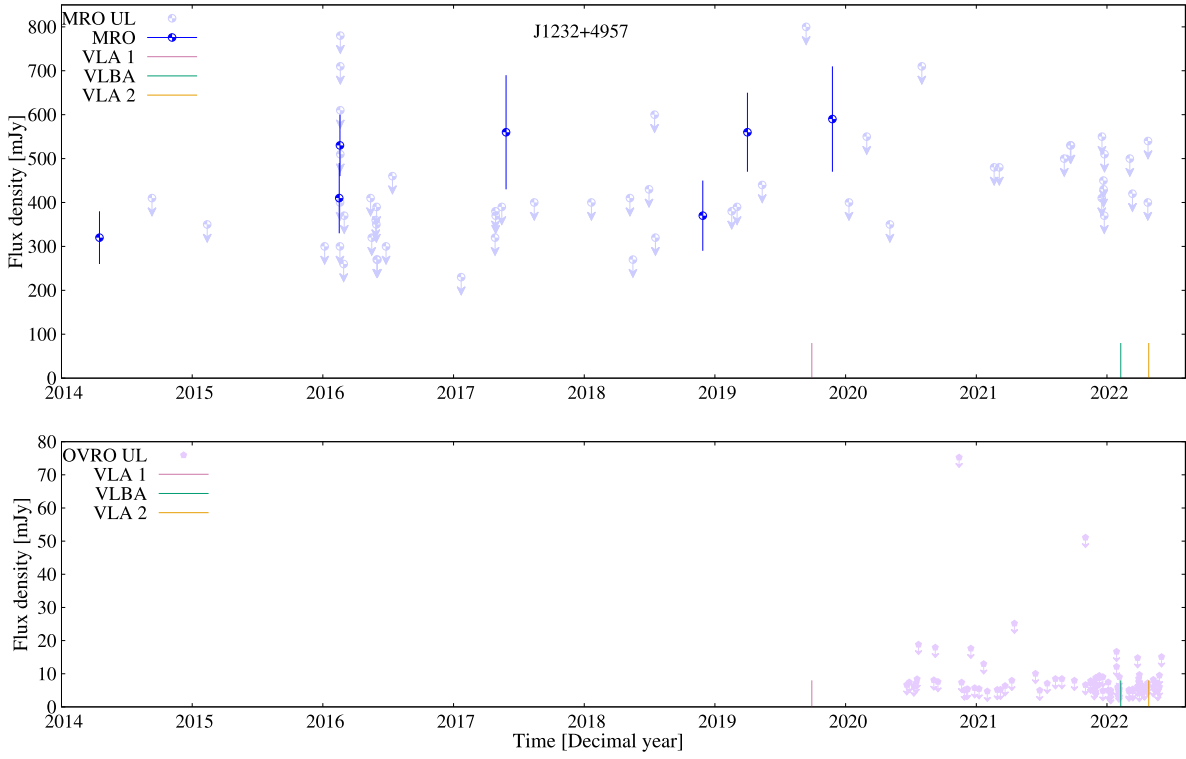


Figure C10. MRO (37 GHz) and OVRO (15 GHz) light curves of J1232+4957. Symbols as in Fig. C8.

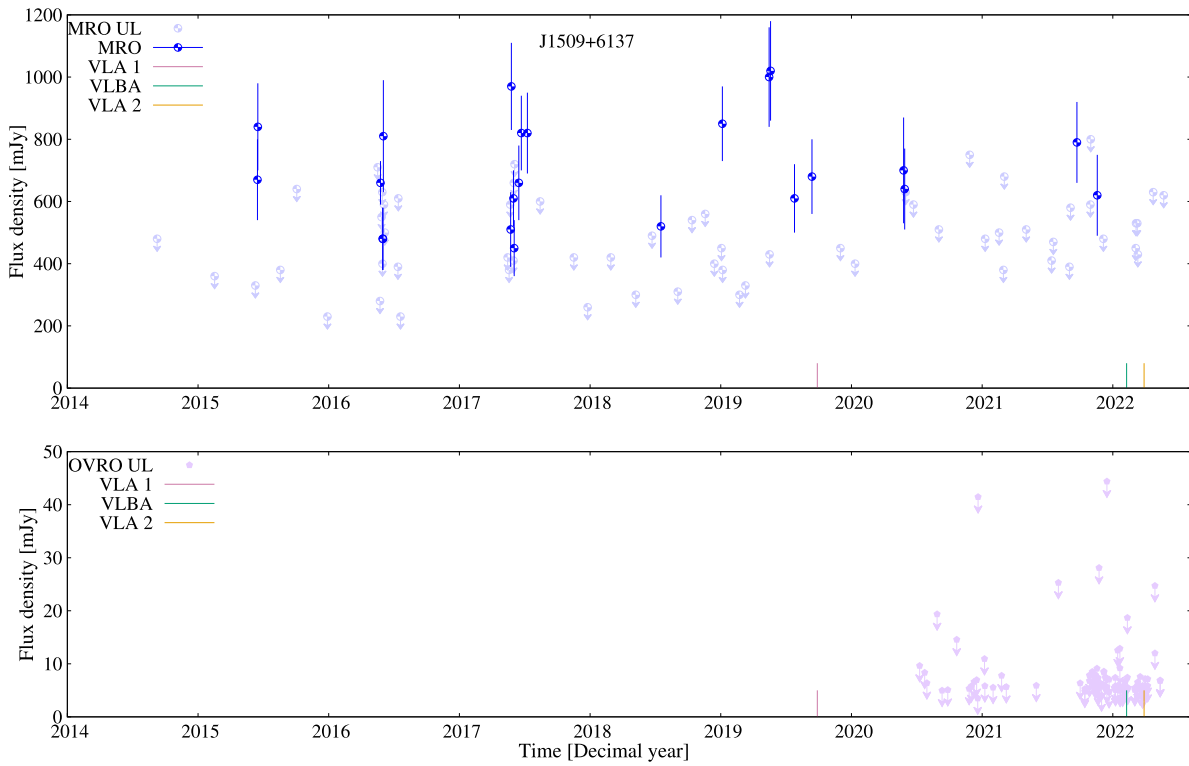


Figure C11. MRO (37 GHz) and OVRO (15 GHz) light curves of J1509+6137. Symbols as in Fig. C8.

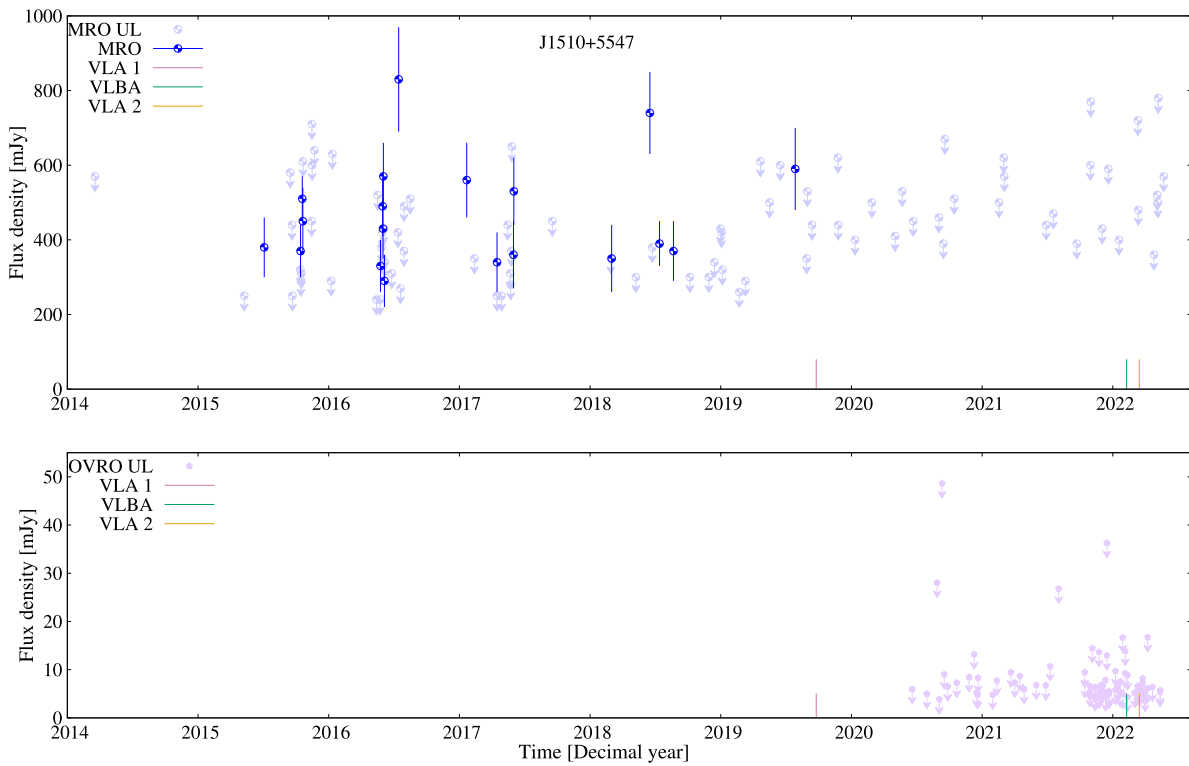


Figure C12. MRO (37 GHz) and OVRO (15 GHz) light curves of J1510+5547. Symbols as in Fig. C8.

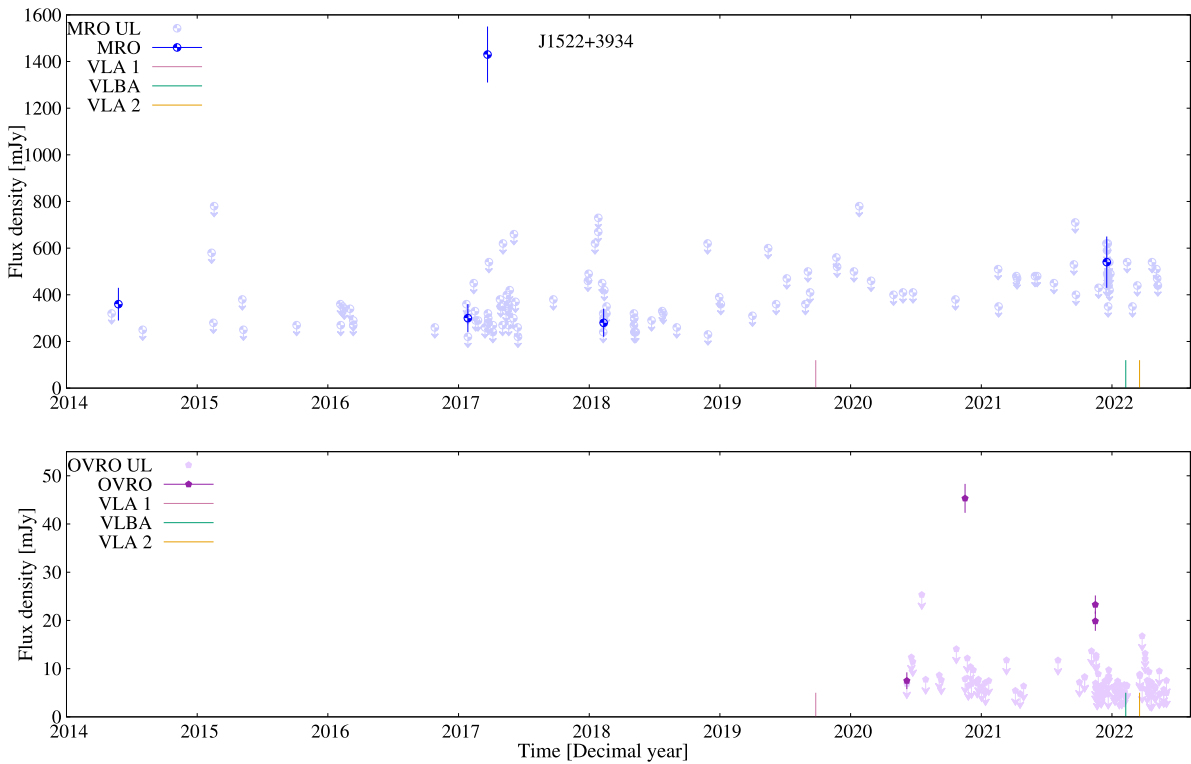


Figure C13. MRO (37 GHz) and OVRO (15 GHz) light curves of J1522+3934. Symbols as in Fig. C8.

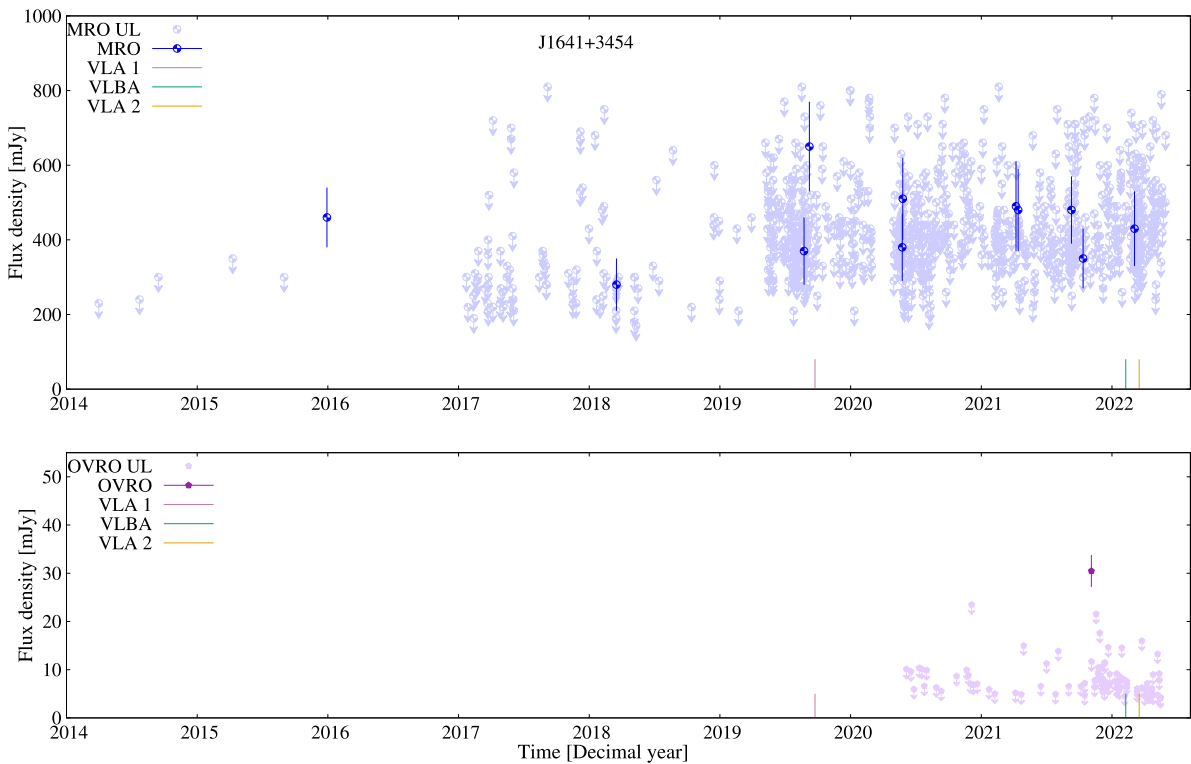


Figure C14. MRO (37 GHz) and OVRO (15 GHz) light curves of J1641+3454. Symbols as in Fig. C8.

This paper has been typeset from a $\text{\TeX}/\text{\LaTeX}$ file prepared by the author.